Journal of Biomolecular Structure and Dynamics

ISSN: 0739-1102 (Print) 1538-0254 (Online) Journal homepage: www.tandfonline.com/journals/tbsd20

Structural and functional characterization of 6-phosphogluconate dehydrogenase in *Plasmodium falciparum* (3D7) and identification of its potent inhibitors

Alagesan Karthika, Nagarajan Hemavathy, Mathimaran Amala, Sundaraj Rajamanikandan, Malaisamy Veerapandian, Dhamodharan Prabhu, Umashankar Vetrivel, Chun Jung Chen, Chitra Jeyaraj Pandian & Jeyaraman Jeyakanthan

To cite this article: Alagesan Karthika, Nagarajan Hemavathy, Mathimaran Amala, Sundaraj Rajamanikandan, Malaisamy Veerapandian, Dhamodharan Prabhu, Umashankar Vetrivel, Chun Jung Chen, Chitra Jeyaraj Pandian & Jeyaraman Jeyakanthan (2024) Structural and functional characterization of 6-phosphogluconate dehydrogenase in *Plasmodium falciparum* (3D7) and identification of its potent inhibitors, Journal of Biomolecular Structure and Dynamics, 42:4, 2058-2074, DOI: 10.1080/07391102.2023.2248271

To link to this article: https://doi.org/10.1080/07391102.2023.2248271

JOURNAL OF BIOMOLECULAR STRUCTURE AND DYNAMICS
2024, VOL. 42, NO. 4, 2058–2074
https://doi.org/10.1080/07391102.2023.2248271

Structural and functional characterization of 6-phosphogluconate dehydrogenase in *Plasmodium falciparum* (3D7) and identification of its potent inhibitors

Alagesan Karthika[a]*, Nagarajan Hemavathy[a,b]*, Mathimaran Amala[a], Sundaraj Rajamanikandan[c], Malaisamy Veerapandian[a], Dhamodharan Prabhu[c], Umashankar Vetrivel[d,e], Chun Jung Chen[f], Chitra Jeyaraj Pandian[g] and Jeyaraman Jeyakanthan[a]

[a]Structural Biology and Bio-Computing Lab, Department of Bioinformatics, Science Block, Alagappa University, Karaikudi, Tamil Nadu, India; [b]Centre for Bioinformatics, Vision Research Foundation, Chennai, Tamil Nadu, India; [c]Centre for Drug Discovery, Karpagam Academy of Higher Education, Coimbatore, Tamil Nadu, India; [d]ICMR-National Institute of Traditional Medicine, Nehru Nagar, Belagavi, Karnataka, India; [e]ICMR-National Institute for Research in Tuberculosis, Chennai, Tamil Nadu, India; [f]Life Science Group, Scientific Research Division, National Synchrotron Radiation Research Center, Hsinchu, Taiwan; [g]Department of Biotechnology, Dr. Umayal Ramanathan College for Women, Karaikudi, Tamil Nadu, India

Communicated by Ramaswamy H. Sarma

ABSTRACT

The malarial parasite *Plasmodium falciparum* predominantly causes severe malaria and deaths worldwide. Moreover, resistance developed by *P. falciparum* to frontline drugs in recent years has markedly increased malaria-related deaths in South Asian Countries. Ribulose 5-phosphate and NADPH synthesized by Pentose Phosphate Pathway (PPP) act as a direct precursor for nucleotide synthesis and *P. falciparum* survival during oxidative challenges in the intra-erythrocytic growth phase . In the present study, we have elucidated the structure and functional characteristics of 6-phosphogluconate dehydrogenase (6PGD) in *P. falciparum* and have identified potent hits against 6PGD by pharmacophore-based virtual screening with ZINC and ChemBridge databases. Molecular docking and Molecular dynamics simulation, binding free energies (MMGBSA & MMPBSA), and Density Functional Theory (DFT) calculations were integratively employed to validate and prioritize the most potential hits. The 6PGD structure was found to have an open and closed conformation during MD simulation. The *apo* form of 6PGD was found to be in closed conformation, while a open conformation attributed to facilitating binding of cofactor. It was also inferred from the conformational analysis that the small domain of 6PGD has a high influence in altering the conformation that may aid in open/closed conformation of 6PGD. The top three hits identified using pharmacophore hypotheses were ChemBridge_11084819, ChemBridge_80178394, and ChemBridge_17912340. Though all three hits scored a high glide score, MMGBSA, and favorable ADMET properties, ChemBridge_11084819 and ChemBrdige_17912340 showed higher stability and binding free energy. Moreover, these hits also featured stable H-bond interactions with the active loop of 6PGD with binding free energy comparable to substrate-bound complex. Therefore, the ChemBridge_11084819 and ChemBridge_17912340 moieties demonstrate to have high therapeutic potential against 6PGD in *P. falciparum*.

ARTICLE HISTORY
Received 21 December 2022
Accepted 9 April 2023

KEYWORDS
Plasmodium falciparum; 6-phosphogluconate dehydrogenase (6PGD); molecular dynamics simulations; pharmacophore-based virtual screening; MMGBSA

1. Introduction

Plasmodium falciparum is a protozoan parasite, and one of the most virulent species of *Plasmodium* that causes malaria in humans. Among the *Plasmodium* genus, five species (*P. falciparum, P. vivax, P. ovale, P. malariae*, and *P. knowlesi)* are known to cause human infections (Antinori et al., 2012). About 229 million cases of malaria infections were reported of which 4,09,000 people died from malaria in 2019 (Gregson & Plowe, 2005; Institute of Medicine (US) Committee on the Economics of Antimalarial Drugs, 2004). According to the World Health Organization (WHO), children under the age of five (57% of malaria fatalities) are the most vulnerable group affected by malaria (WHO Report Malaria, 2020). Malarial transmission is predominantly mediated through the bite of female *Anopheles* mosquitoes (Figure 1). The initiation of host infection primarily occurs in the liver and replicates within hepatocytes (Kaushansky et al., 2013; Pimenta et al., 2015). Wherein, after release into the bloodstream, it gets multiplied inside human red blood cells (RBCs) through asexual replication, and egress from infected RBCs (Figure 1) (Dhangadamajhi et al., 2010). Then, the parasite crosses the midgut epithelium, multiplies, reaches the salivary gland (SG) epithelium, and further gets transmitted to the next human host (Aly et al., 2009).

Plasmodium parasites have developed resistance to several front-line antimalarial drugs (aryl amino alcohol, antifolate, and artemisinin compounds), and in recent years,

CONTACT Jeyaraman Jeyakanthan jjbioinformatics@gmail.com
*These authors equally contributed to the work.
Supplemental data for this article can be accessed online at https://doi.org/10.1080/07391102.2023.2248271.
This article has been corrected with minor changes. These changes do not impact the academic content of the article.

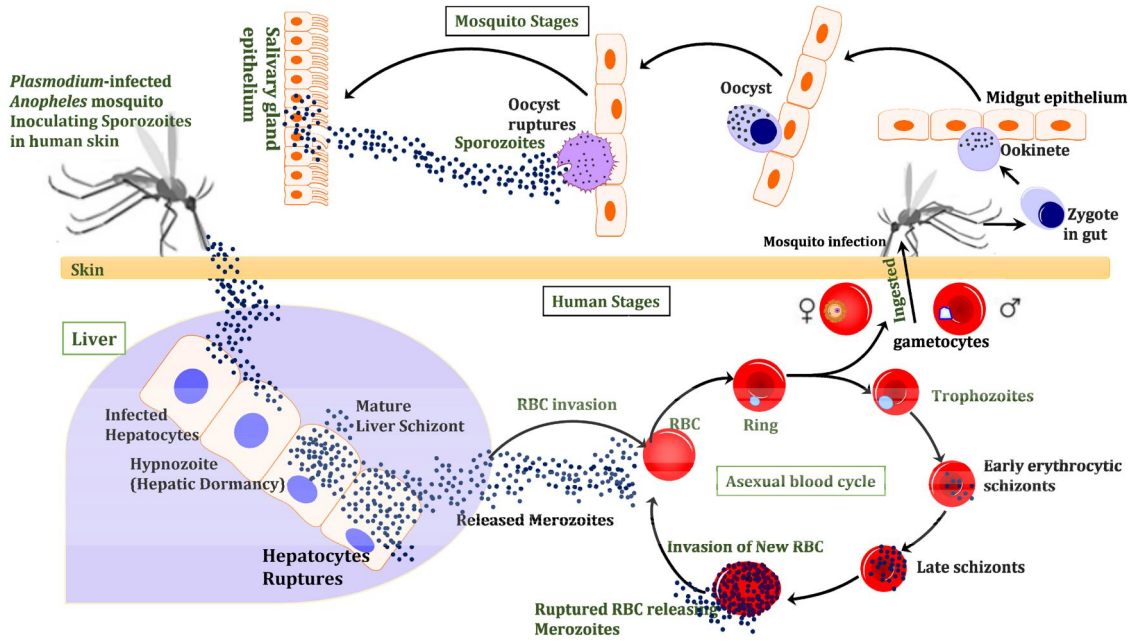

Figure 1. Representation of *P. falciparum's* life cycle in mosquito and human host.

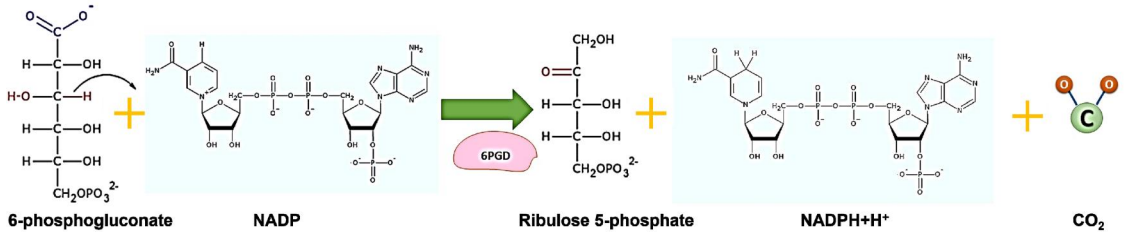

Figure 2. Oxidative decarboxylation reaction catalyzed by 6-phosphogluconate dehydrogenase (6PGD).

resistance to combination therapies using artemisinin has also increased (Cowell & Winzeler, 2019; Huthmacher et al., 2010; Nosten & White, 2007; Shibeshi et al., 2020). Hence, there is a dearth to identify novel antimalarial agents. There are several malarial enzymes and pathways, such as nucleic acid metabolism, redox metabolism, and oxidative stress that can serve as promising drug targets for designing antimalarial drugs (Chen et al., 2019; Litwack, 2018; Nepveu & Turrini, 2013). In *Plasmodium,* the Pentose Phosphate Pathway (PPP) serves as the main source for the synthesis of ribulose 5-phosphate and NADPH, wherein it provides reducing equivalents for downstream glutaredoxin (Grx) and thioredoxin (Trx) dependent reactions, which are essential for antioxidant defense, redox balance, redox regulation and cell growth of parasites (Stincone et al., 2015). These redox systems help the parasites to survive in extraordinary conditions, as it can withstand the oxidative challenges that they encounter during their intra-erythrocytic growth (Becker et al., 2004). Hence, targeting redox metabolism can be a potential drug target.

In general, the PPP consists of two arms, a unidirectional oxidative arm followed by a non-oxidative arm. In *P. falciparum,* the PPP (*Pf*PPP) is initiated by the bifunctional enzyme glucose 6-phosphate dehydrogenase and 6-phosphogluconolactonase (G6PD/6PGL). It catalyzes the conversion of glucose 6-phosphate into 6-phosphogluconate, with the production of one NADPH molecule (Ayala et al., 1991). The PPP of *P. falciparum* is different from humans, wherein the reaction is catalyzed by two different enzymes G6PD and 6PGL. The second enzyme of the *Pf*PPP is 6-phosphogluconate dehydrogenase (6PGD) which catalyzes the third step of the oxidative arm to produce ribulose 5-phosphate (RuP) by oxidative decarboxylation of 6-phosphogluconate (6PG) and one additional NADPH molecule (Figure 2). In the non-oxidative arm, it will undergo several enzymatic reactions and primarily produce Ribose 5-phosphate (R5P) followed by fructose 6-phosphate. The conversion of 6PG to RuP is essential for many eukaryotic organisms. Besides, the PPP produces ribose, which is the direct precursor for nucleotide synthesis. In addition, the generated NADPH supplies electrons for nucleotide, lipid, and fatty acid biosynthesis (Boros et al., 1998; Kesebir et al., 2022; Yıldız et al., 2022). Moreover, inhibition of this PPP may cause a crucial effect on the parasite's survival. Suppression of PPP will cause cell death and hinder the generation of NADPH and RuP formation. Hence, the second enzyme (6PGD) of *Pf*PPP was considered a crucial target for antimalarial drug design in this study. Besides, this enzyme structure and active site counterparts are varied from human 6PGD thus making it a potential target for antimalarial drugs (Preuss et al., 2012).

Also, developing 6PGD inhibitors is a promising way to combat the malarial pathogen *P. falciparum*.

The 6PGD family of proteins is a functional homodimer and contains a cofactor ($NADP^+$) and a substrate (6PG) binding site. The structural architecture of 6PGD illustrates that $NADP^+$ binding is occupied in the small domain (SD; composed of βαβ), while the substrate-binding occurs in the larger domain (LD; composed of α helixes). The C-terminal residues play a major role in linking the two monomers of the dimer. Both $NADP^+$ and substrate binding are independent of each other, however, substrate binding plays a crucial role in catalysis and therefore the site is targeted to identify potent 6PGD inhibitors. Still, the optimal binding of the cofactor at the small domain of the 6PGD enzyme is yet to be probed. There were several *in silico* studies on the targeted enzymes which proves the importance of targeting 6PGD enzymes for therapeutics. In an *in silico* and *in vitro* study on 6PGD, the effect of methyl 4-amino benzoates was evaluated and it showed good binding score and IC50 value (Kesebir et al., 2022). In an another study, through molecular docking and competitive inhibitor identification analysis, fluorophenyl thioureas has been demonstrated to show better binding interaction with 6PGD (Yıldız et al., 2022). In one of the studies, scaffold-based and De novo based molecule identification based on the parietin was used to identify inhibitors against 6PGD. Using a De novo based approach they have generated molecules that would fit better in a 6PGD pocket (Çalışkan et al., 2022). The anti-depression drug effect (aripiprazole, mirtazapine, risperidone, escitalopram, and haloperidol) on inhibiting 6PGD was also studied and it was found to have a significant effect (Özaslan et al., 2019). Rhodanines obtained from green synthesis were tested against 6PGD and it was found to be effective (Karaman et al., 2020). Though there are many studies about 6PGD in different organisms, still there is a lack of clear insights on targeting 6PGD in *P. falciparum*. Henceforth, various computational methods were implemented in this study to understand the crucial residues that influence the open and close conformation of the 6PGD enzyme, besides deciphering the optimal binding of the cofactor at the small domain. High-throughput screening approach to drug discovery has received significant attention in recent years due to its specificity, accuracy, and sensitivity to real-time counterparts. Therefore, the pharmacophore-based screening of compounds was also implemented, followed by various filtration analyses to prioritize the hits that may act as effective drug moiety for combating malarial pathogens (*P. falciparum* 3D7).

2. Materials and methods

In the present study, 6-phosphogluconate dehydrogenase (PF14_0520) (6PGD) of *P. falciparum* (isolate 3D7) was prepared using Schrödinger's Protein Preparation Wizard. The pre-processed structures of *apo* and *holo* (complexed with cofactor and substrate) forms of 6PGD were considered for molecular dynamics (MD) simulations to probe their structural stability and conformational changes using the GROMACS suite. Subsequently, Free Energy Landscape (FEL) and Principal Component Analysis (PCA) were used to identify representative near-native conformations from MD simulations. Furthermore, the substrate-bound near-native conformation was considered for pharmacophore-based virtual screening against the both ZINC and ChemBridge database to identify potent hits.

2.1. Protein preparation

Three-dimensional structures of 6-phosphogluconate dehydrogenase enzyme (Uniprot Id: Q8IKT2) are available in three states namely *apo* 6PGD (PDB ID: 6FQX), 6PGD in complex with NAP (cofactor) (PDB ID: 6FQY), and 6PGD in complex with 6-phosphogluconate (substrate) (PDB ID: 6FQZ) (Haeussler et al., 2018). All these structures were pre-processed using the Protein Preparation Wizard (2021) of the Schrödinger suite to optimize the stereochemical features by assigning proper bond order, removing steric clashes, adding hydrogen atoms, fixing the disulfide bonds, missing residues, atoms, and loops. The structures were further energy minimized using Optimized Potentials for Liquid Simulations (OPLS3) force field. Refinement was performed by adjusting the terminal chi rotation of Asparagine, Glutamine, and Histidine residues. The minimization ends when the root mean square deviation (RMSD) of heavy atoms exceeds 0.3 Å in the minimized structure relative to X-ray structural coordinates.

2.2. Molecular docking

The enzyme 6PGD normally requires $NADP^+$ as a cofactor for catalysis, yet the available cofactor-bound 6PGD structure (PDB ID: 6FQY) has adenine-dinucleotide phosphate but lacks ribose-bound Nicotinamide moiety (Haeussler et al., 2018). There is a structural difference of NAP (cofactor) in complex with 6PGD and $NADP^+$ (Figure S1). Therefore, to infer the flexible binding of nicotinamide in the $NADP^+$ binding site, molecular docking was performed. Initially, the $NADP^+$ (CID-5586) retrieved from the PubChem database (Kim et al., 2016) was prepared through the Ligprep (2021) module to generate its respective tautomers with proper chiralities, and ring conformations using the OPLS3 force field (Jorgensen & Tirado-Rives, 1988). The receptor grid for $NADP^+$ was generated with default parameters around the NAP interacting residues of 6PGD (Leu9, Ala10, Met12, Asn31, Arg32, Thr33, Arg36, Ile74, Lys75) obtained from the ligplot of the crystal structure (PDB ID: 6FQY) (Yıldız et al., 2022). The docking was performed using the SP (Standard Precision) mode of the Schrödinger suite (Halgren et al., 2004). The highest scoring pose was selected and used for further analysis.

2.3. Molecular dynamics simulations

MD simulations were performed using GROMACS 5.1.4 (Van Der Spoel et al., 2005) package with Gromos53A6 as a force field. The initial structure of enzymes was centered in a cubic environment of 1 nm distance and solvated with the SPC water model (Oostenbrink et al., 2004). Then, the solvated

systems were neutralized and energy was minimized using the steepest descent minimization for 50,000 steps. During these steps, the coulombs and van der Waals interactions were maintained at a cut-off of 0.9 nm and 1.0 nm, respectively. Next, the systems were equilibrated under canonical ensemble (NVT) and isothermal-isobaric ensemble (NPT) using Leap-frog integrator for 100 picoseconds (ps) (Nguyen et al., 2014). The system was maintained using a Berendsen thermostat (temperature coupling) and a Berendsen barostat (pressure coupling) at 300K and 1 bar, respectively. Long-range electrostatics were maintained by Particle-Mesh Ewald (PME) and short-range electrostatics were maintained by coulombs and van der Waals at a cut-off 1.0 nm each at a time-step of 10 femtoseconds (fs). LINCS algorithm (AIP Conference Proceedings, 1992; Hess, 2008) was used to maintain the geometry of the molecules. The well-equilibrated system was then subjected to MD simulations for 100 nanoseconds (ns) each at 300 K without any constraints, where the conformations were sampled at an interval of 2 ps (Nagarajan et al., 2022). Finally, the trajectories were analyzed using GROMACS utilities to probe the conformational changes, fluctuations, compactness, and stability of the enzyme complexes (Karthika et al., 2021).

Moreover, to estimate the global concerted movement which represents the functional behavior of the enzyme, Principal Component Analysis (PCA) and Free Energy Landscape (FEL) analysis were performed (Surekha et al., 2016). Further, from the resulting minimum energy cluster of the enzymes, a representative structure of the near-native conformation was used for further studies. Subsequently, to visualize the direction of movement based on the projection of Eigenvectors, porcupine plots were generated using the ProDy (Protein Dynamics and sequence analysis) (Maisuradze et al., 2009) plugin of the VMD (Visual Molecular Dynamics) package (Humphrey et al., 1996). Since elasticity is considered one of the intrinsic properties of proteins, the protein angular dispersion (PADω) which is denoted as one of the quantitative descriptions was determined for each residue using T-Pad analysis (Caliandro et al., 2012). The PADω was calculated to reveal the backbone transitions by applying directional statistics on the Ramachandran angles obtained from MD simulations to analyze the backbone transitions, infer the flexible or rigid residues, and identify the transition states.

2.4. Pharmacophore modeling and validation

The set of 9 antimalarial compounds from Haeussler et al. (2019), was used as a scaffold for generating the Common Pharmacophore Hypothesis (CPH) using PHASE (Choubey & Jeyaraman, 2016; Dixon et al., 2006). Initially, the compounds were prepared with the Ligprep (2021) module and were subjected to the PHASE module which utilizes scoring techniques and fine-grained conformational sampling to identify CPH. For pharmacophore feature generation, the maximum number of features per hypothesis was set to 4-5 and other parameters were set to default. Besides, all the prepared compounds were allowed to generate conformers, while a maximum of 50 best conformers was retained per ligand. Torsion driving approaches were used to generate the conformers for the ligands and energy minimization was performed using Merck Molecular Force Field (MMFFs), with an implicit GB/SA solvent model. Six types of pharmacophore feature namely hydrogen bond acceptor *(A)*, hydrogen bond donor *(D)*, hydrophobic group *(H)*, negatively ionizable *(N)*, positively ionizable *(P)*, and aromatic ring *(R)* were used to define the chemical structural patterns. A tree-based partitioning technique was used to identify CPH for a set of variants. The CPHs were scored by setting the RMSD and vector scores to 1.0 and 0.5, respectively. The highest survival and fitness score was used to characterize the best CPHs and to determine the quality of the model. Prior to enrichment analysis and validation, the decoys of the known inhibitors (9 antimalarial compounds) were generated using the RADER server (Wang et al., 2017). Whereas the decoys were generated for each known inhibitor, the Tanimoto threshold for the active vs decoy and decoy vs decoy was set as 0.75 and 0.90, respectively. The generated decoys further prepared by the LigPrep module were selected for validating the resulting CPHs using enrichment analysis and the Boltzmann-enhanced discrimination of the receiver operating characteristic (ROC) curve.

2.5. Pharmacophore-based virtual screening

The validated CPHs were used to identify potential hit molecules against 6PGD of *P. falciparum*. The library of one million compounds from the ZINC and ChemBridge databases were prepared and energy minimized using the OPLS3 (Jorgensen & Tirado-Rives, 1988) force field with the Ligprep (2021) module. Further, the prepared compounds were screened based on the validated CPH, whereas the resulting hits were ranked based on RMSD suite matching, vector alignments, and volume terms. In addition, the resultant hits should satisfy the essential pharmacophoric features identified in the CPHs. The hits showing the highest fitness and survival score were taken for molecular docking studies. Finally, the optimized ligand datasets were considered for virtual screening against the near-native conformation of the 6PGD-6PG complex. The receptor grid was generated around the substrate (6PG) binding residues of 6PGD using the Receptor Grid Generation module of Schrödinger. Initially, the hits were subjected to Glide High-throughput virtual screening (Friesner et al., 2004, 2006; Halgren et al., 2004). The hits that bind to the substrate-binding site of 6PGD with a better Glide score were passed to the next stage of Standard Precision (SP) docking. Finally, 20% of the hits retrieved from SP were subjected to the Extra Precision (XP) docking. The hits with poor pharmacological properties were eliminated using QikProp (2021) filters including Lipinksi's rule of five, the number of rotatable bonds, and ADME (absorption, distribution, metabolism, and excretion) properties (Rajamanikandan et al., 2017). The resulting hits were taken for further analysis.

2.6. Prioritization of hits

The top 50 compounds obtained from XP docking were subjected to Prime MM-GBSA (Molecular Mechanics, the Generalized Born Model, and Solvent Accessibility) analysis to determine the binding free energies for the protein-ligand complexes. The binding free energy calculation was carried out using the following equation (Equation (1)) (Prime, 2021).

$$\Delta G_{bind} = G_{complex} - (G_{protein} + G_{ligand})$$
$$G = EMM + GSGB + GNP \quad (1)$$

where the $G_{complex}$ is the complex energy, $G_{protein}$ is the receptor energy, G_{ligand} is the unbound ligand energy, EMM represents molecular mechanics energies, GSGB is an SGB solvation model for polar solvation, and GNP is a nonpolar solvation term. Interaction energy was also calculated from the MacroModel script which calculates the component energies of interacting atoms between the protein and ligand. Finally, the top three hits with better pharmacological properties and the least toxicity were shortlisted for Density functional theory (DFT) calculations and MD simulations.

2.7. Density functional theory

Density functional theory (DFT) calculations were performed for the selected hits using the Jaguar module of Schrödinger (Jaguar, 2021). Becke's three-parameter exchange potential and Lee-Yang-Parr correlation functional (B3LYP) method with a basis set of 6-31 G* were used for ligand geometry optimization (Amala et al., 2019; Becke, 1993). Poisson-Boltzmann Solvers equation was used for energy minimization. HOMO (Highest Occupied Molecular Orbitals), LUMO (Lowest Unoccupied Molecular Orbitals), and energy gaps were calculated for the hit molecules (Lee et al., 1988).

2.8. Binding free energy calculations based on MMPBSA

In addition, the binding free energies for *holo* forms were calculated using the molecular mechanics/Poisson Boltzmann surface area (MM/PBSA) approach using the g_mmpbsa tool of Gromacs. The contribution of each residue towards binding free energy was calculated using the MmPbSaDecomp.py python script. The solvation-free energy was calculated using an implicit solvent model. It is the combination of electrostatic terms, estimated by solving the Poisson–Boltzmann (PB) equation and the non-polar solvation energy, separated as attractive and repulsive interaction. Moreover, based on the per-residue interaction analysis, the energy contributed by each residue for the stable interactions of the complex was also determined.

3. Results and discussion

3.1. Molecular docking of cofactor to 6PGD

The docking analysis of $NADP^+$ to 6PGD (Figure S2(a)) at chain A and chain B resulted in a Glide score of −8.38 kcal/mol and −7.10 kcal/mol, respectively. From the interaction analysis (Figure 3(a,b)), it was inferred that the residues namely Arg36, Gly451, and Glu131 showed H-bond interactions in both chains of 6PGD. Furthermore, $NADP^+$ adopts different binding orientations within the binding site of 6PGD in both subunits. The residue Arg36, which is highly specific to *P. falciparum* was found to form an H-bond interaction with the hydroxyl group of phosphate (PA) in chain A, and H-bond interaction with an oxygen atom (P3) and the hydroxyl group of R2 in chain B. In addition, residues namely, Asn31, Asn83, and Gly100 showed prominent H-bond interactions in subunit A, whereas the residues Lys75, Lys182, Asn102, and Arg32 form H-bond interaction with subunit B. The strong π-cation interaction was found to be formed by the residue Arg32 with $NADP^+$ in both subunits. From our observation, the crystal structure with NAP and docked $NADP^+$ has shared only one common interaction, i.e. with the Arg36 amino acid. Overall from the results, it was observed that the ribose and nicotinamide moiety of $NADP^+$ is more flexible at the binding site of 6PGD, thereby aiding $NADP^+$ in adopting different conformation in the two subunits.

3.2. Molecular dynamics simulation

3.2.1. Probing the conformational and fluctuation changes of apo and holo forms of 6PGD

The dimeric *apo* 6PGD (Figure S2(b)) in the RMSD plot showed higher deviations of dimeric state than the subunits chain A and chain B (Figure S3(a)). However, the dimeric form attained equilibrium after ∼60 ns and maintained deviations of about ∼ 0.45 nm. Among the subunits, chain A has shown the least deviations, and both chains were stabilized after ∼62 ns. Regarding the domain-based RMSD analysis (Figure S3(b,c)), it was observed that the high deviations of chain A were attributed specifically to the C-terminal (∼0.24 nm) in the last 40 ns, while the small domain (SD) and large domain (LD) attained least deviations. In the case of chain B, the C-terminal showed the least deviations from the other domains, and all domains were found to be converged in the last 20 ns. In the case of the 6PGD-$NADP^+$ complex, the RMSD of the overall dimeric state was observed to have the same deviations (∼0.4 nm) as that of subunit A, while both the chains attained equilibrium and converged after ∼50 ns (Figure S3(a)). LD and C-terminal region (Figure S4(b,c)), attained higher deviations of ∼0.35 nm and ∼0.3 nm in chain A and chain B, respectively, which can be attributed to the deviations of the respective chains throughout the MD production run. In trajectory analysis of the 6PGD-PG complex (Figure S2(c)), the dimeric form was observed to attain higher deviations than that of chain A (∼0.35 nm) and chain B. However, the complex was found to have maintained equilibrium after 25 ns till the end of the MD production run (Figure S5(a)). Whereas, on analyzing the domain-specific RMSD, the C-terminal was observed to have higher deviations (∼0.3 nm) than the other domains in chain B, while the least deviations were observed by the domains of chain A (Figure S5(b,c)). On comparative backbone RMSD analysis of *apo* and *holo* forms of 6PGD (Figure 4(a–c)), it was observed that 6PGD in complex with substrate 6PG has shown the

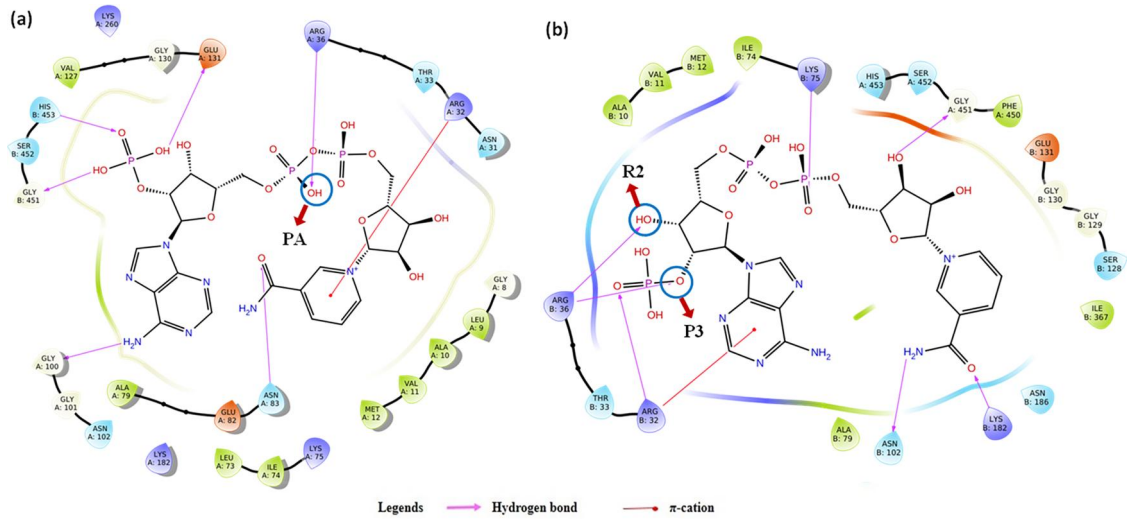

Figure 3. (a) 2D interaction plot of NADP$^+$ with chain A of 6PGD (b) 2D interaction plot of NADP$^+$ with chain B of 6PGD.

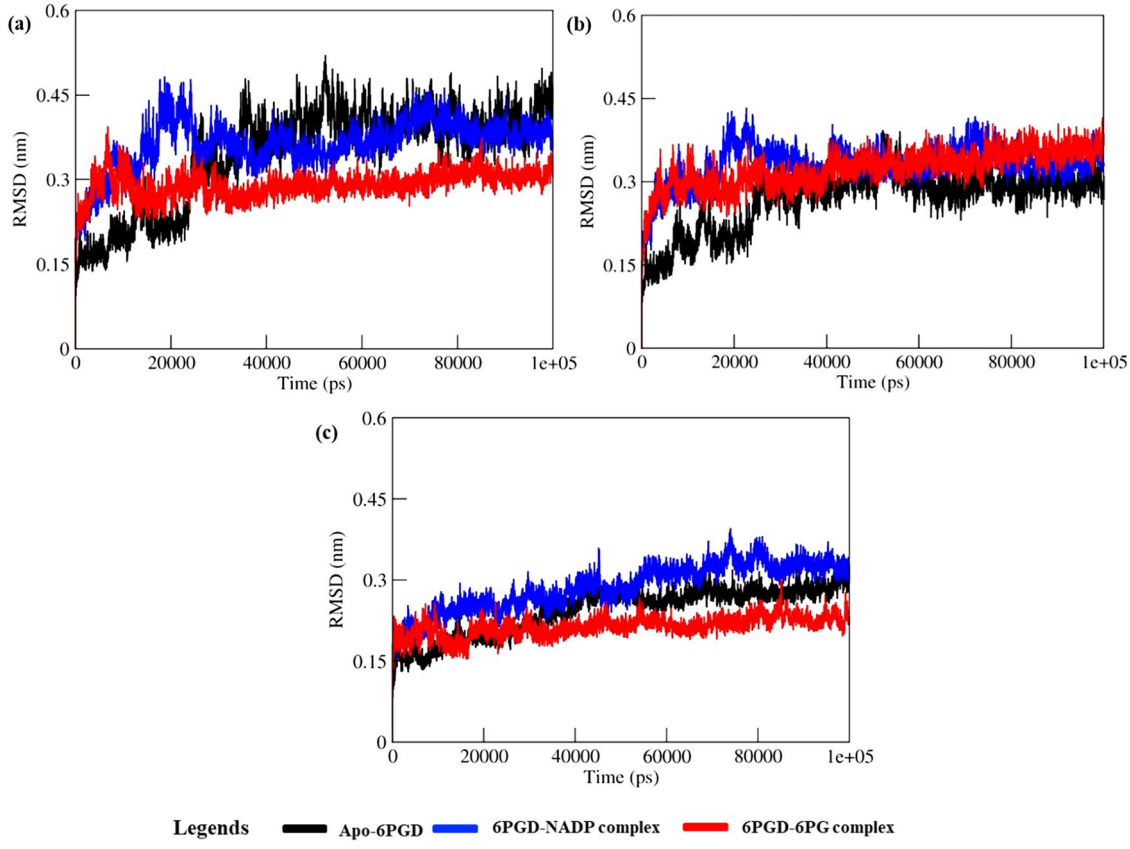

Figure 4. Comparative backbone RMSD analysis of 6PGD (a) Overall (both apo and holo forms), (b) chain A, and (c) chain B.

least deviations (∼0.3 nm) than the *apo* and NADP$^+$ *holo* form. In addition, the 6PGD-6PG complex was found to be well equilibrated after ∼25 ns and has maintained its convergence throughout the MD production run. After ∼24 ns, the *apo* 6PGD has shown drastic deviation (∼0.45 nm) as that of the 6PGD-NADP$^+$ complex and has maintained throughout, however, both the trajectories have converged in the last 20 ns of the MD production run. Wherein, chain A in both *apo* and *holo* forms did not show any deviations, and were observed to be well equilibrated. Whereas in chain B, only the 6PGD-NADP$^+$ complex has shown higher deviations (∼0.3 nm) suggesting that chain B of cofactor bound 6PGD is highly flexible than the *apo* and *holo* form bound with the substrate (6PGD-6PG).

From the RMSF plot of *apo* 6PGD (Figure S3(d–f)), it was observed that expect for C-terminal residues, major fluctuations were observed in chain B than in chain A. In specific, the loop conferring residues Gly77 (∼0.64 nm), Pro78 (∼0.77 nm) of SD, and the LD residues Thr262 (∼0.4 nm) that spans in the activation loop and Asn317 (∼0.48 nm) were observed. Besides, the Asn382 (∼ 0.41 nm) which aids in the stability of the dimeric state was also found to fluctuate in

chain B than in chain A. On contrary, the chain A residues were observed to have higher fluctuations than chain B of the 6PGD-NADP$^+$ complex. Since the residues namely, Glu46 (∼0.72 nm) and Asn313-Glu314 (∼0.47-0.48 nm) spanning SD and LD were observed to show higher fluctuations (Figure S4(d–f)). In the case of the 6PGD-6PG complex, the major fluctuations were attained by chain B, specifically in SD residues namely Glu46 (∼0.501 nm), Lys116 (∼0.546 nm), and Asn317 (∼0.44 nm) of LD (Figure S5(d–f)). However, on the comparative analysis (Figure 5(a–d)), it was inferred that the 6PGD in complex with NADP$^+$ has shown higher residual flexibility than the 6PGD *apo* and 6PG *holo* forms. Overall, it has been observed that the SD residues of both chain A and chain B have shown higher fluctuations than other domains in *apo* and *holo* forms except for the 6PGD-6PG complex. In particular, the SD residues namely Pro78 and Glu46 were found to have higher fluctuations in *apo* and NADP$^+$ bound form, respectively. While the residue Asn382 that spans in the LD region enhancing the stability of the dimeric state was found to have higher fluctuations only in the *apo* form than the *holo* forms.

3.3. Conformational compactness and altered molecular motion analysis

The radius of the gyration plot (Figure 6a) showed that the *apo* form has maintained its compactness without attaining any conformational changes. Among the *holo* forms, the 6PGD-6PG complex has shown a higher degree of compactness of about ∼2.56 nm, while, the 6PGD-NADP$^+$ complex has attained open conformation with the least degree of compactness than *apo* and 6PG *holo* forms. Besides, the open and closed conformations of 6PGD at the substrate-binding site could be attributed to the distance between the activation loop [a.l] (Asp255-Thr262) and C-terminal loop (c.l) (Gly451-Arg460) surrounding the other side of the substrate-binding site. It was inferred from the distance plot (Figure 6(b,c)), that the *apo* 6PGD maintained a distance of about ∼3.2 nm between the loops. While in the 6PGD-NADP$^+$ complex, the distance between a.l. and c.l. is highly drastic than the 6PGD-6PG complex, since it has maintained an increased distance of about ∼3.5 nm and ∼3 nm in chain A and chain B, respectively. On comparative analysis of the *apo* and the *holo* forms, it was observed that the 6PGD-6PG complex has shown the least distal deviations between a.l and c.l by maintaining an average distance of about ∼2.7 nm and ∼2.5 nm in chain A and chain B, respectively. Distance analysis evidenced that the 6PGD-6PG complex has shown closed conformation, while the 6PGD-NADP$^+$ complex showed a higher degree of open conformation than the *apo* form. Moreover, from the mode vector analysis of the *apo* and *holo* forms (Figure 7(a–c)), in the 6PGD-6PG complex, the a.l was observed to have a higher magnitude of inward movement, while the small domain showed a drastic inward motion towards the large domain thereby decreasing the feasibility of small domain to accommodate the cofactor NADP$^+$. Whereas 6PGD in *apo* form and complex with NADP$^+$ was observed to have outward protrusion of a.l and c.l in the substrate-binding site, thereby attaining the open conformation. The least disruption of a.l along with the small domain increases the likelihood of cofactor binding in the small domain. The result of the study evidenced that the substrate-bound conformation attains inward movement of

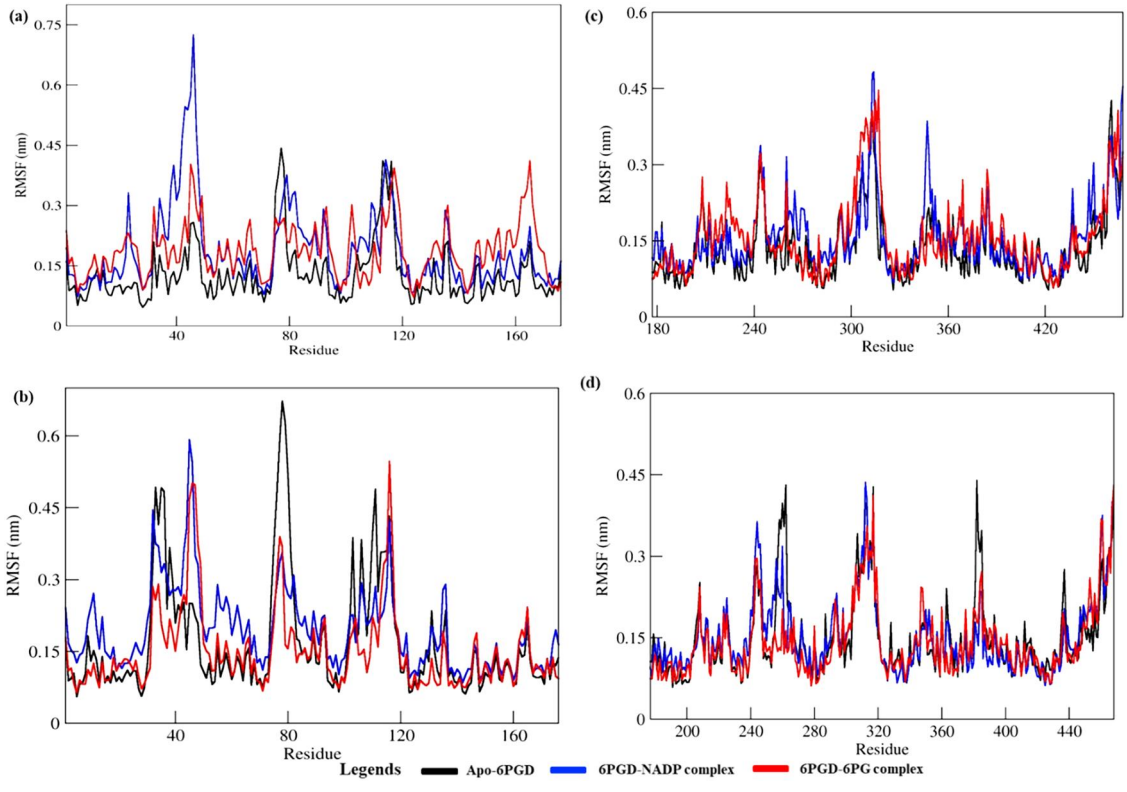

Figure 5. Comparative RMSF analysis of 6PGD *apo* and *holo* forms: chain A (a) small domain (c) large domain; chain B (b) small domain (d) large domain.

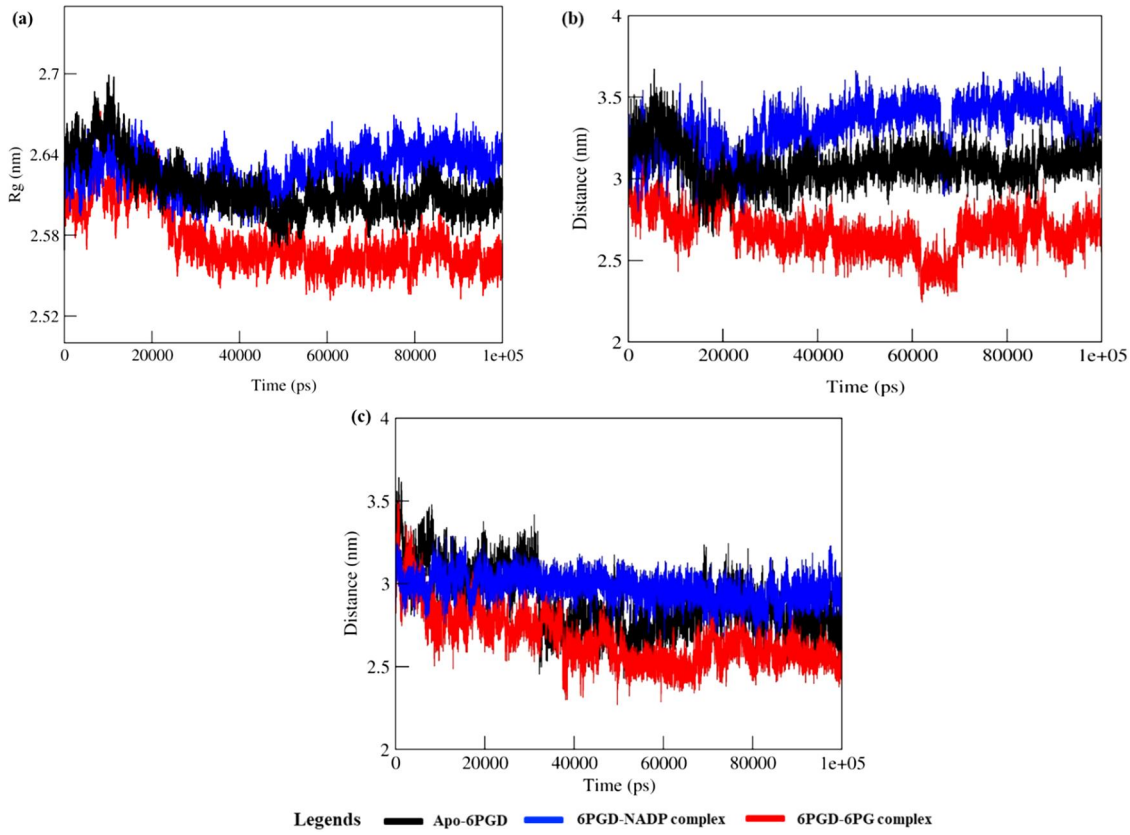

Figure 6. Comparative MD analysis of G6PD *apo* and *holo* form, (a) compactness analysis based on the radius of gyration plot; Distance plot of substrate binding cavity (b) chain A (c) chain B.

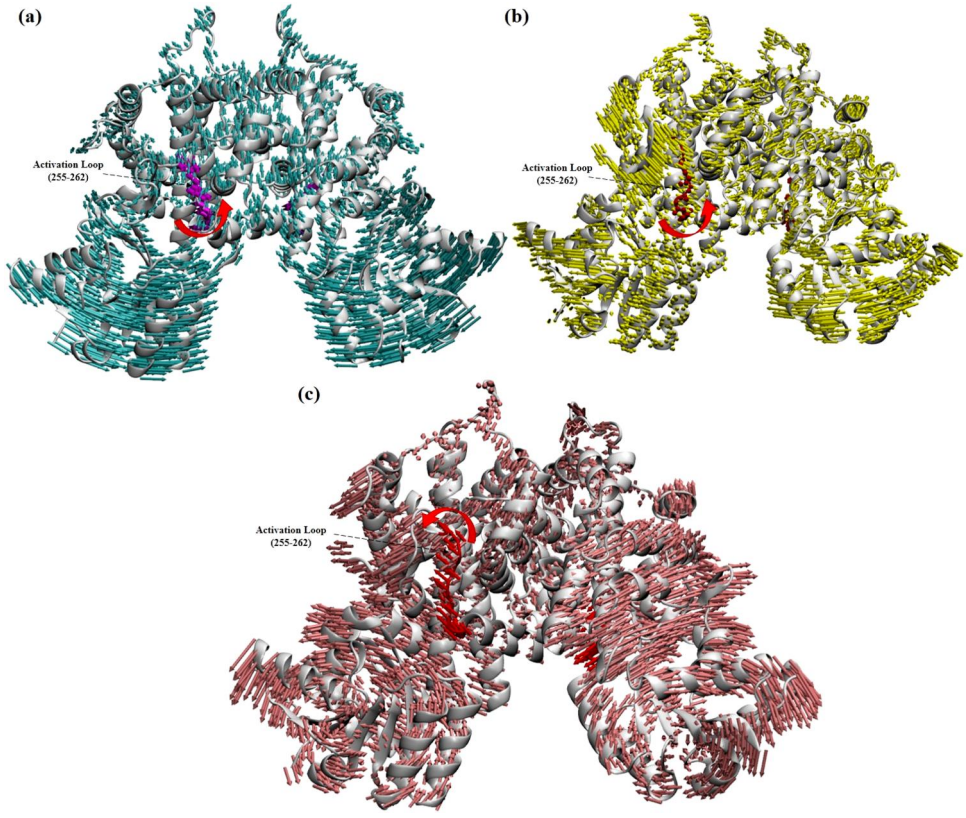

Figure 7. Porcupine plots of 6PGD *apo* and *holo* form, (a) *apo* 6PGD, (b) 6PGD-$NADP^{+}$ complex, and (c) 6PGD-6PG complex, where the direction of arrows indicates the direction of motion of the protein and the length indicating the magnitude of motion. The direction of movement of activation loop residues is indicated by arrows (red).

a.l contributing to the interaction of substrate, while the $NADP^+$ bound state attains outward movement of a.l, which relaxes the small domain facilitating binding of the cofactor, $NADP^+$.

3.4. Secondary structure analysis

On analyzing the secondary structural changes of the *apo* 6PGD (Figure S6(a,b)), the α helix (Trp104-Glu117) was found to have drastically transformed as turns in both subunits. This transformation is highly crucial since the Trp104 residue aids in altering the conformation of 6PGD on interacting with Trp265 (spanning the a.l) to attain higher flexibility and leads to prominent conformational changes that alter the binding of cofactor and substrate. Apart from that, prominent structural changes were observed in chain B, with the loss of α helices in the small domain (Tyr34-Glu47; Pro78-His90) and β turn (Arg457-Arg460) of the C-terminal region which maintains the stability of the dimeric state by penetrating the adjacent chain A. The chain A of the 6PGD-$NADP^+$ complex after approximately 25 ns completely transformed into turns (Trp104-Glu117). In chain B also, the helix (Ser139-Ser159) has changed into turns after 65 ns. Both the chains showed partial bends in the α helix (Tyr34-Glu47) spanning the small domain and facilitating $NADP^+$ interaction after 52 ns. From the secondary structural changes plot of the 6PGD-PG complex (Figure S8(a,b)), it was observed that the α helix (Trp104-Glu117) was observed to be sparsely transformed as bends after ∼20 ns in both chains. While a prominent loss of ' α helix' (Tyr34-Glu47) was observed in chain A at the end of the 20 ns period.

3.5. Conformational changes and structural transitions of apo and holo forms of 6PGD

Based on the PCA and FEL analysis the representative structures of their near-native conformation were extracted at 81.79^{th} ns (*apo*), 58.9^{th} ns (6PGD-NADP), and 73.99^{th} ns (6PGD-6PG) (Figure S9). On comparative structural analysis of initial and near-native conformation of the *apo* form (Figure 8(a–d)), it was observed that the α helical segments that were transformed as loops namely Leu73-Ala79 were found to have a prominent inward movement towards the cavity in both the chains. Moreover, the active loop (Asp255-Thr262) has shown an outward movement in both the chains than the initial conformation. The crucial active site residue Lys260 was also found to be protruding outwards in both chains. In addition, it was also inferred from the T-PAD analysis (Figure S10(a–c)) that the residue Gly258 spanning the active loop has attained higher fluctuations of about 164.59°, while the α helix (Trp104-Lys118) residing residues have shown transitions in specific residue Asn102 with the maximum transition of 131.79° denoting the high probability of secondary structure transition of α helix. However, the key residues Trp104, Lys260, and Trp265 have shown the least intensity of fluctuations. While the comparative structural analysis of initial and near-native conformation of 6PGD-$NADP^+$ (Figure 9(a–d)), has shown the inward motion of sparsely transformed α helix (Trp104-Lys118), especially Trp104. However, the α helix (Trp104-Lys118) spanning residues have the least degree of short transitions (Figure S11(a–c)), whereas the active loop residue, Ile256 was observed to have higher fluctuations of 146.75°. The major displacement was shown by the residue Lys260 which was observed to have a higher degree of short transitions of about 118.55° than the *apo* form. Though chain A has maintained the stable hydrogen bonds of about ∼8 with $NADP^+$ throughout the simulation, while chain B has shown fewer stable H-bonds with $NADP^+$ (Figure S12(a)), only fewer stable H bonds were observed in the near-native conformation of the 6PGD-$NADP^+$ complex (Figure S13(a,b)). The key residue which has a prominent role in cofactor interaction, Met12, Arg32, Thr33, and Arg36 of 6PGD have maintained their stable H-bond interactions with $NADP^+$. In specific, the active loop residing residue Thr262 of chain B has formed stable interaction with $NADP^+$. In the case of the 6PGD-6PG complex, only Glu461 residue has shown higher fluctuations of ∼132.64° (Figure S14(a–c)), while the least intensity of transitions or fluctuations was attained by the residues in this substrate-bound 6PGD complex. However, it was observed from the 6PGD-6PG comparative structural analysis (Figure 10(a–d)), that the loop (Val126-Ala132) showed a prominent inward movement towards the substrate in both the chains, specifically the residue Gly128 has an inward protrusion and has higher feasibility of forming favorable interaction with the substrate than that of the initial conformation. Moreover, the active loop (Asp255-Thr262) has shown an inward movement in both the chains than the initial conformation. However, the N-atom of Lys260 forming crucial interaction with the substrate was found to be in closer proximity to the substrate in chain A than chain B. From the inter-hydrogen interaction plot (Figure S12(b)), it was observed that chain A has maintained an increased number of H-bonds with the substrate (∼15 H-bonds) than chain B. While the substrate interactions (Figure S15(a,b)) of near-native conformation showed that chain A has maintained the H-bonds formed by the key residues namely Lys182, Asn186, and Lys260 with 6PG as that of the initial conformation, thereby aiding the stability of the complex.

3.6. Pharmacophore-based screening and prioritization of hit compounds

The AARR model was selected based on scoring functions and alignment with antimalarial compounds. As depicted in the AARR hypothesis, the two aromatic *(R)* regions and two acceptors *(A)* regions are mapped onto the antimalarial compounds (Figure 11). The selected hypothesis was further validated, which showed a ROC of 0.51, an RIE of 0.19, and an Area under the accumulation curve of 0.63. The best hypothetical AARR model was used as a 3D structural search query for retrieving potent molecules from the ZINC and ChemBridge database which resulted in 89,761 and 5,79,117 hits, respectively, on PHASE screening. The resultant hits had a fitness score in the range of −0.75 to 2.445, which satisfied the defined pharmacophore hypothesis. Furthermore, the

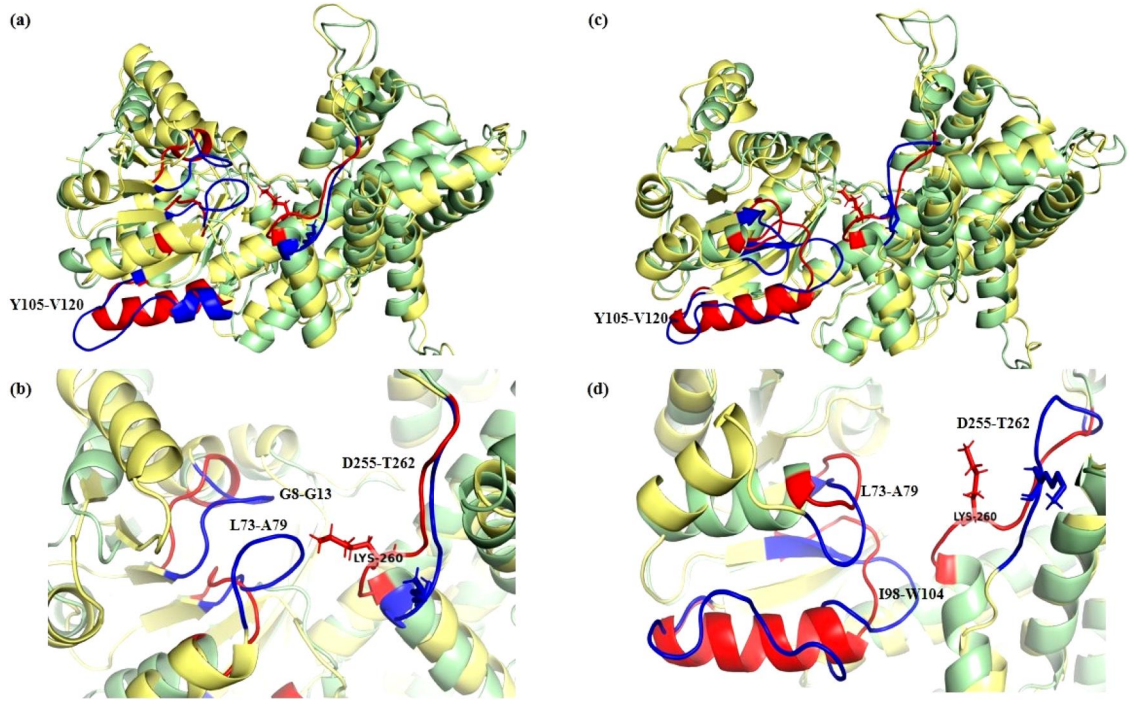

Figure 8. Comparative structural analysis of initial (pale green colour) and near-native conformation (Wheat colour) of *apo* 6PGD (a) chain A (b) representing the changes occurring around the cavity of chain A (c) chain B (d) representing the changes occurring around the cavity of chain B; where the changes in initial are shown in red colour, while in near-native conformation the changes are shown in blue.

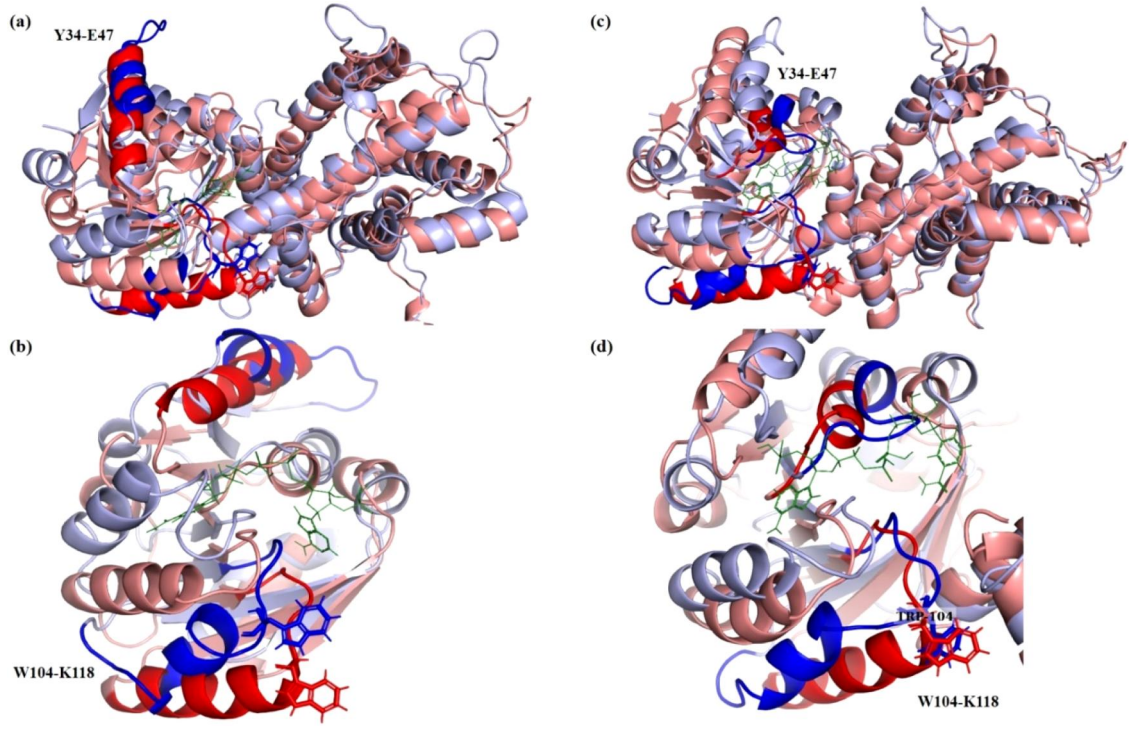

Figure 9. Comparative structural analysis of the initial (Salmon colour) and the near-native conformation (pale blue colour) of 6PGD-$NADP^+$ complex (a) chain A and (b) the structural changes occurring around the cavity of chain A (c) chain B and (d) the structural changes occurring around cavity of chain B; where the changes in initial are shown in red colour, while in near-native conformation the changes are shown in blue.

resultant hits were taken for virtual screening against 6PGD. The XP resultant hits were prioritized based on a Glide score in the range of −9.13 kcal/mol to −7.46 kcal/mol and were considered for MMGBSA analysis. Based on overall scoring functions, the top 5 hits were shown in Table 1. Though the ZINC compounds (ZINC1085692166 and ZINC972575255) showed a good glide score of −9.13 kcal/mol and −8.55 kcal/mol, they showed unfavorable outcomes in ADMET prediction (Table 2). The $Qplog_{HERG}$ and QPP_{Caco} were not in the admissible range. Therefore, the next top three hits from ChemBridge with good ADMET properties were considered for further analysis.

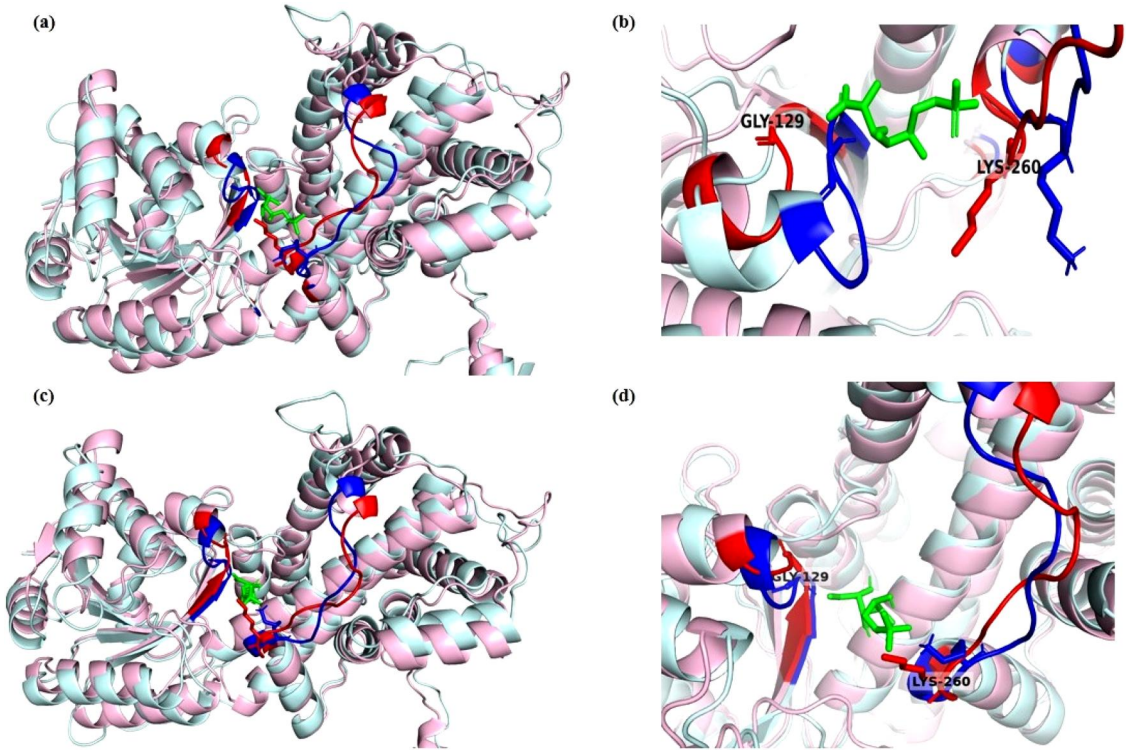

Figure 10. Comparative structural analysis of the initial (pale Pink colour) and near native conformation (pale cyan colour) of 6PGD-6PG complex (a) chain A (b) representing the changes occurring around the cavity of chain A (c) chain B (d) representing the changes occurring around the cavity of chain B; where the changes in initial are shown in red colour, while in near-native conformation the changes are shown in blue.

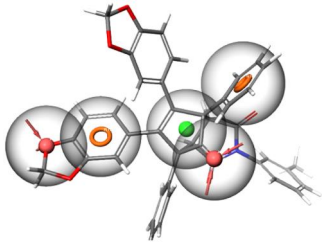

Figure 11. Identified pharmacophoric features in the antimalarial compounds.

Table 1. Glide scoring functions for the identified hits.

S. No	Compound ID	Gscore kcal/mol	GEnergy kcal/mol	GEmodel kcal/mol	Prime MMGBSA kcal/mol
1	ZINC1085692166	−9.13	−41.53	−55.8	−30.99
2.	ZINC972575255	−8.9	−49.36	−65.06	−49.19
3	ChemBridge_11084819	−8.51	−47.6	−57.37	−38.41
4	ChemBridge_17912340	−7.5	−47.52	−56.63	−32.25
5	ChemBridge_80178394	−7.46	−41.72	−51.4	−39.65

All three hits showed the Glide score, Glide energy, and Glide Emodel in the range of −8.51 kcal/mol to −7.46 kcal/mol, −47.60 kcal/mol to −41.72 kcal/mol, and −57.37 kcal/mol to 51.25 kcal/mol, respectively. ChemBridge_11084819 ([5-[(2,4-dioxoimidazolidin-1-yl)methyl]-3-(2-methoxybenzyl)-1H-1,2,4-triazol-1-yl]acetic acid) showed the highest scoring function and formed eight H-bonds interactions with the 6PGD enzyme (Figure 12(a)). The carboxyl group of ChemBridge_11084819 formed seven H-bond interactions with the amine group of Arg447 (C = O···HN, bond length = 1.89 Å), Arg287 (C = O···HN, bond length = 2.36 Å), Lys260 (C–O···HN, bond length = 1.82 Å), Gly261 (C–O···HN, bond length = 2.40 Å), Gly129 (C = O···HN, bond length = 2.17 Å), Gly130 (C = O···HN, bond length = 2.63 Å) and Asn186 (C = O···HN, bond length = 2.51 Å). Additional H-bond interaction was observed between the carboxyl and hydroxyl group of hit and Thr262 (C = O···HO, bond length = 2.06 Å). In case of ChemBridge_17912340 (2-[(3R,4S)-3-[[3-(pyrazol-1-ylmethyl)benzoyl]amino]oxan-4-yl]oxyacetic acid), the carboxyl group of hit forms H-bond interactions with the amine group of Lys75 (C = O···HN, bond length = 2.30 Å), Lys182 (C-O···HN, bond length = 1.84 Å), Lys260 (C-O···HN, bond length = 2.59 Å), Gly261 (C = O···HN, bond length = 2.01 Å), Thr262 (C = O···HN, bond length = 1.93 Å), Gly263 (C = O···HN, bond length = 2.58 Å) and Arg447 (C-O···HN, bond length = 2.77 Å) (Figure 12(b)). Similarly, ChemBridge_80178394 (N-[3-[(5-methylpyridin-2-yl)amino]propyl]-2-oxo-3H-1,3-benzoxazole-5-sulfonamide) showed the least Glide score of −7.46 kcal/mol among the three hits selected with five H-bond interactions (Figure 12(c)). The amine group of the hit showed two H-bond interactions with the carboxyl group of Glu131 (NH···O = C, bond length = 1.57 Å & 2.41 Å). The sulphonate group of ChemBridge_80178394 showed two H-bond interactions with the amine group of Lys182 (S = O···HN, bond length = 2.01 Å) and Lys260 (S = O···HN, bond length = 1.96 Å), and the carboxyl group of hit showed H-bond interaction with the amine group of Thr262 (C = O···HN, bond length = 1.99 Å). All three hits showed conserved salt-bridge interaction with the residue Arg447. In addition, ChemBridge_80178394 and ChemBridge_11084819 showed salt-bridge interactions with Glu131 and Lys182 amino acid residues. From the interaction analysis of these hits with 6PGD, it was inferred that all the hits have shown hydrogen bonds with Lys260, and Thr262 which are known to be the crucial residues that favor substrate-binding.

Table 2. Pharmacological properties for the hits predicted through QikProp.

S. No	Compound_ID	Mol. W	QPlogpW	QPlogPo/W	QPlogS	$Qplog_{HERG}$	QPP_{Caco}	% HOA
12	ZINC1085692166	292.3	12.06	−0.06	−1.83	−5.06	19.27	56.92
2.	ZINC972575255	292.3	16.28	−1.45	−0.78	−5.0	14.53	39.26
3.	ChemBridge_11084819	359.34	13.64	1.40	−2.81	−2.71	21.22	58.89
4.	ChemBridge_17912340	359.38	14.08	2.06	−2.45	−2.50	161.59	78.54
5.	ChemBridge_80178394	362.40	16.10	0.87	−3.73	−4.74	52.65	62.85

Mol. W:<500, QplogpW: -4.0 to 45.0, QplogPo/W: -2.0 to 6.5, QplogS: -6.5 to 0.5, $Qplog_{HERG}$: below -5.0, QPP_{Caco}: <25 poor >500 great, % HOA – <25% poor >80% High.

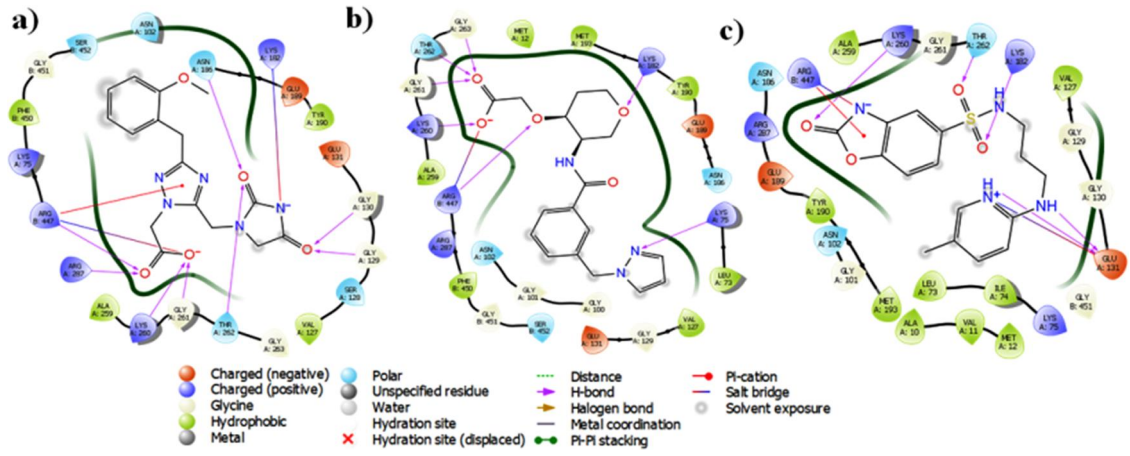

Figure 12. 2D interaction of hits identified from ChemBridge database (a) ChemBridge_11084819 (b) ChemBridge_17912340 (c) ChemBridge_80178394.

Table 3. Interaction profile of hits inside the binding site of 6PGD.

S. No	Compound_ID	Hydrophobic interaction	H-bond interaction	Π-cation	Salt bridge
1.	ChemBridge_11084819	A:Lys260	A:Gly129, Gly130, Asn186, Lys260, Gly261, Thr262, Arg 287; B:Arg447	B:Arg447	A:Lys182 B:Arg447
2.	ChemBridge_17912340	A: Val127	A:Lys75, Lys182, Lys260, Gly261, Thr262, Gly263 B:Arg447	–	B:Arg447
3.	ChemBridge_80178394	A: Ala10, Ile74	A:Glu131, Lys182, Lys260, Thr262	B:Arg447	A:Glu131 B:Arg447

In specific, all three have shown strong π-cation interaction with the Arg447 residue (Table 3).

3.7. Density functional theory

The HOMO and LUMO orbitals for the hits were characterized and plotted (Figure 13). HOMO and LUMO are directly associated with ionization potential and electron affinity, respectively (Wang et al., 2017). The energy gap calculated between HOMO and LUMO determines the chemical stability. Besides, the observed low energy gap between the orbitals depicts high reactivity, low stability, and implicitly high polarizability of the molecules. The calculated HOMO, LUMO values, and energy gap for the hits range from −0.23 eV to −0.20 eV, −0.07 eV to 0.00 eV, and 0.21 eV to 0.12 eV, respectively, indicating fragile nature of the bound electrons. Analysis of the HOMO map of ChemBridge_80178394 indicates that HOMO energies are located in 1,3 benzoxazole and the LUMO map was distributed in the 5-methyl pyridine. In the case of ChemBridge_17912340, HOMO distribution was observed in the carboxyl, oxygen atom, and amine groups, where the LUMO are located in pyrazol-1-ylmethyl benzoyl. The distribution of HOMO and LUMO energies for ChemBridge_11084819 was located on the dioxoimidazolidin and 2-methoxybenzyl, respectively. The distribution of molecular orbitals provides additional evidence of possible reactive sites in the molecules. In the comparison of docking studies and DFT, the observed reactive sites played a major role in forming hydrogen bond interactions with 6PGD. distribution of hits identified from ChemBridge database (a-b) ChemBridge_11084819 (c-d) ChemBridge_17912340 (e-f) ChemBridge_80178394.

3.8. Molecular dynamics-based stability analysis of the complexes

The overall backbone RMSD plot of the complexes (Figure 14(a)) showed that 6PGD in complex ChemBridge_17912340 showed similar deviations (∼0.3 nm) as that of the 6PGD-6PG complex, while both have attained equilibrium after 20 ns and have maintained till the MD production run. In the case of other complexes, 6PGD in complex with

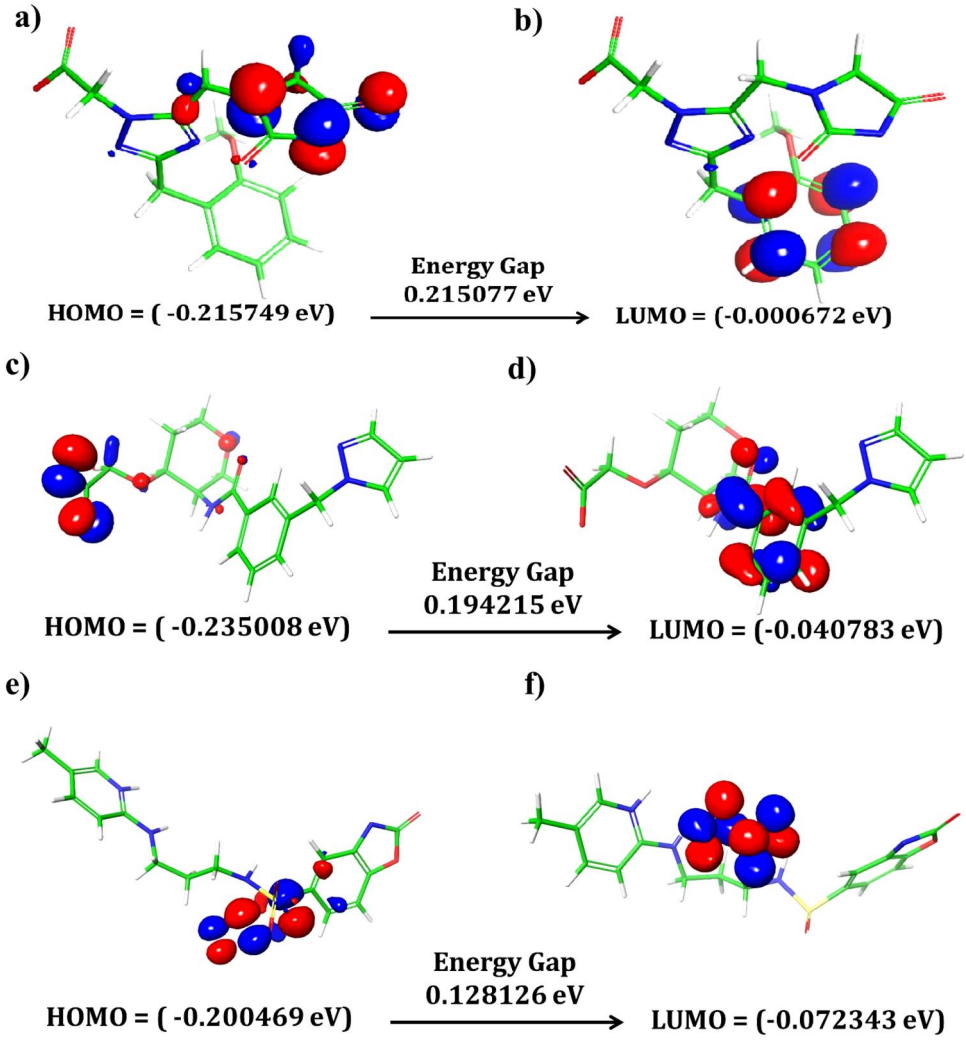

Figure 13. HOMO, LUMO distribution of hits identified from ChemBridge database (a-b) ChemBridge_11084819 (c-d) ChemBridge_17912340 (e-f) ChemBridge_80178394.

ChemBridge_11084819 and ChemBridge_80178394 have shown the least deviations (~0.25 nm) than the 6PGD-6PG complex and have converged in the last ~40 ns. On analyzing the compactness of complexes (Figure 14(b)), it was observed that only the 6PGD-ChemBridge_11084819 complex has maintained its conformation without any change in its compactness, while other complexes have attained an increased degree of compactness. From the inter hydrogen plot (Figure 14(c)), it was observed that the ChemBridge_11084819 has initially increased H bonds with 6PGD (~11 H-bonds), however, only 7 stable H bonds were maintained throughout the MD production run. Among the complexes, ChemBridge_80178394 has maintained only 3 stable H-bond with 6PGD, while compounds ChemBridge_17912340 and ChemBridge_11084819 have seven stable H bonds with 6PGD, thereby maintaining the stability of the complexes. The decrease in the number of H-bonds with ChemBridge_80178394 was substantiated by the distance plot (Figure 14(d)), which shows drastic distal deviations from the active loop attributing to favorable interactions of the substrate. Whereas other compounds (ChemBridge_17912340 and ChemBridge_11084819) and the substrate (6PG) have maintained a proximal distance to the active loop for stable interactions. In terms of the residue fluctuations (Figure 15), it was observed that small domain residues have shown higher fluctuations than large domain. Among the complexes, 6PGD in complex with substrate has shown higher fluctuation of residues than other complexes, yet the loop conferring residues were found to be fluctuating in other complexes.

3.9. Interaction analysis and binding free energy analysis of the complexes

From the interaction analysis (Figure 16 and Table 4) of the near-native conformation of the complexes (Figure S16(a–c)), the interaction with Thr262 was found to be maintained in all the three complexes. However, it was inferred that the residue Lys260 which forms a crucial interaction with substrate is maintained only in 6PGD complexes (ChemBridge_17912340 and ChemBridge_11084819), while the major interaction of active loop residues was observed to be maintained only in the 6PGD-ChemBridge_11084819

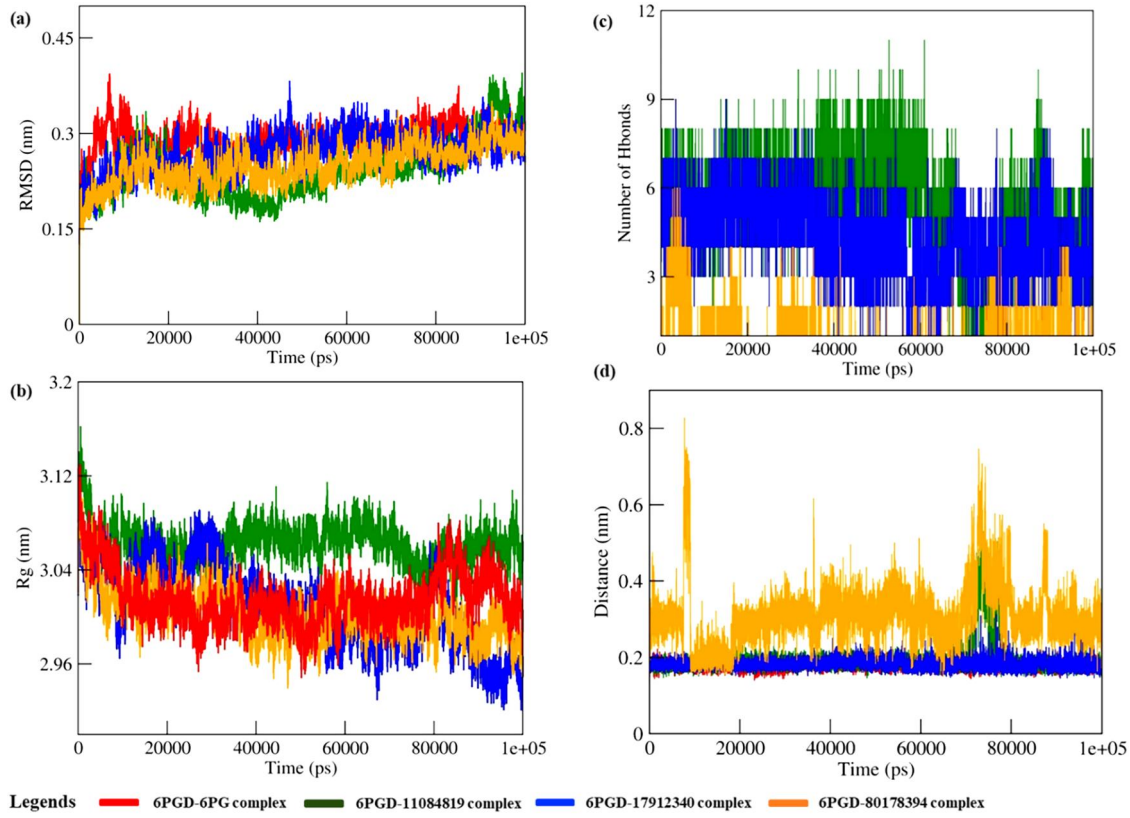

Figure 14. Comparative MD analysis of 6PGD in complex with 6PG complex and top 3 compounds (a) Overall backbone RMSD (b) Radius of gyration (c) inter-hydrogen bonds (d) distance plot between the compounds and the active loop.

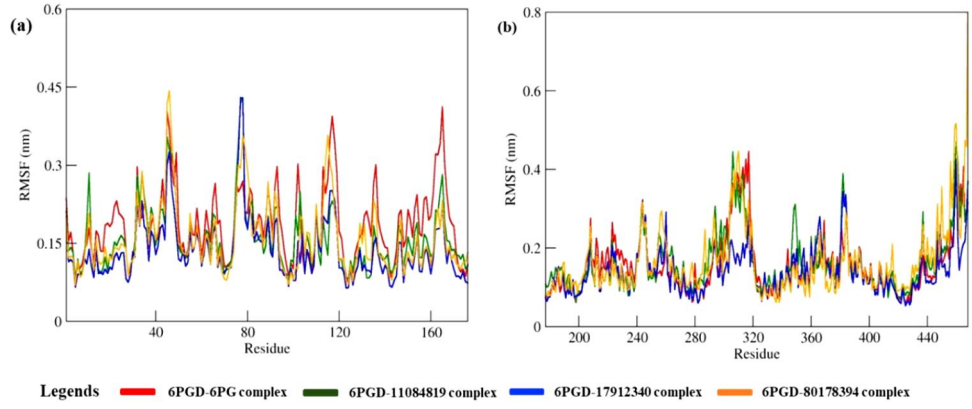

Figure 15. Comparative RMSF analysis of 6PGD in complex with 6PG complex and top 3 compounds of chain A (a) small domain and (b) large domain.

complex. Moreover, the binding free energy analysis (Table 5) of the complexes also showed that the complex 6PGD-ChemBridge_11084819 had higher binding energy than other complexes, and also the binding energy was near to that of the substrate-bound complex. Among the complexes, the 6PGD-ChemBridge_80178394 complex was observed to have the least binding energy, since they have weak van der Waals than the other complexes. Besides the per residue interaction analysis (Figure 17) of the complexes, also showed that higher interactions were observed in the 6PG complex than in the other complexes. However, among the other complexes, residues Lys260, Lys264, and Arg287 were found to have higher interaction in 6PGD complexes (ChemBridge_17912340 and ChemBridge_11084819), whereas the 6PGD-80178394 complex showed the least residual interactions.

4. Conclusion

*Pf*PPP of 6PGD was considered a potential antimalarial drug target, and conformational changes attributed to cofactor or substrate were also observed. As a result of docking cofactor to 6PGD, it was determined that the ribose and nicotinamide moiety of NADP + is more flexible, thereby achieving a diverse conformation in both subunits but maintained H-bonds with conserved residues. Conformational analysis of *apo* and *holo* forms in MD analysis inferred that the 6PGD-6PG complex was better equilibrated than others. Whereas,

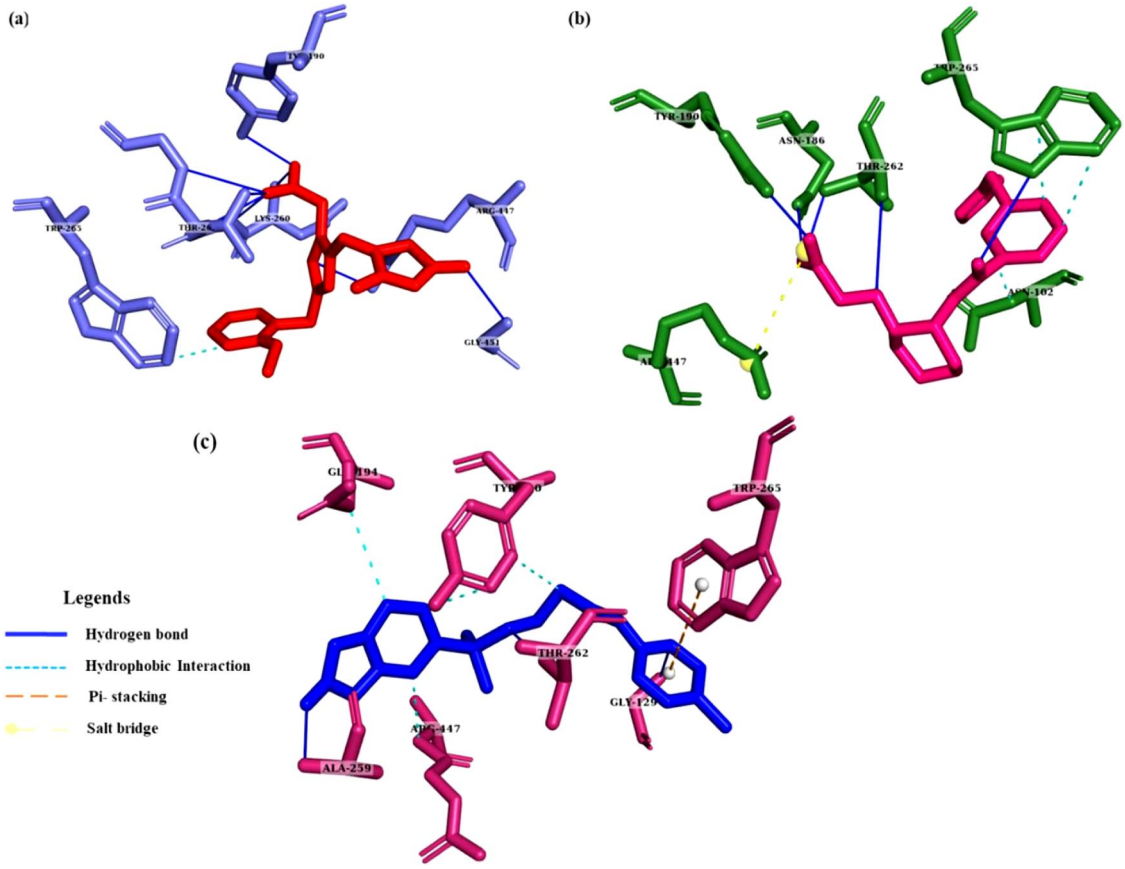

Figure 16. Interaction analysis of near-native complexes of top 3 compounds with 6PGD obtained from PLIP (a) ChemBridge_11084819 (b) ChemBridge_17912340 (c) ChemBridge_80178394.

Table 4. Interactions profile of hits to the near-native conformation complexes.

S.No	ChemBridge_ID	Hydrophobic interaction	H-bond interaction	Π-stacking	Salt bridge
1.	ChemBridge_11084819	A: Trp265	A: Tyr190, Lys260, Gly261, Thr262, Gly263; B: Arg447, Gly451	–	–
2.	ChemBridge_17912340	A: Asn102, Trp265	A: Asn102, Asn186, Tyr190, Thr262, Trp265	–	B: Arg447
3.	ChemBridge_80178394	A: Tyr190, Gln194; B: Arg447	A: Gly129, Ala259, Thr262	A: Trp265	–

Table 5. Binding free energy analysis of the 6PGD complexes.

Complex	Van der Waals energy (kJ/mol)	Electrostatic energy (kJ/mol)	Polar solvation energy (kJ/mol)	SASA energy (kJ/mol)	Binding energy (kJ/mol)
6PGD-6PG	−34.079 ± 2.843	−1125.557 ± 19.465	1008.462 ± 24.070	−11.090 ± 0.186	−162.431 ± 11.911
6PGD-11084819	−131.231 ± 5.725	−309.707 ± 8.638	347.092 ± 7.856	−15.432 ± 0.252	−109.550 ± 5.750
6PGD-17912340	−141.951 ± 3.905	−20.345 ± 2.512	87.797 ± 4.364	−14.662 ± 0.326	−89.177 ± 4.441
6PGD-80178394	−91.337 ± 2.975	−306.202 ± 8.988	358.649 ± 8.418	−12.820 ± 0.215	−51.961 ± 3.570

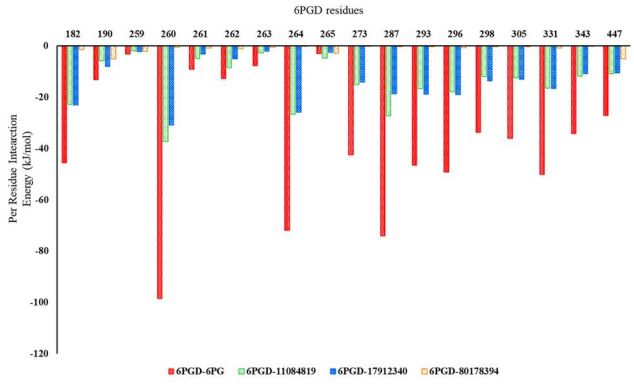

Figure 17. Per residue interaction analysis of 6PGD in complex with the substrate and the top 3 compounds.

the small domain residues were observed to have higher fluctuations because the α helix (Trp104-Glu117) transformed as a loop. This may lead to prominent conformational changes that alter the binding of the cofactor and substrate with 6PGD. The higher degree of compactness in the 6PGD-6PG complex has led to closed conformation, while the outward protrusion of a.l and c.l has led to open conformation in $NADP^+$, thereby increasing the possibility of cofactor binding in *apo* 6PGD and $NADP^+$. The best three hits based on the hypothesis AARR namely, ChemBridge_11084819, ChemBridge_80178394, and ChemBridge_17912340 showed higher glide scores, MMGBSA, and better ADMETox properties. Furthermore, from the MD, it was inferred that the compounds ChemBridge_11084819 and ChemBridge_17912340

to feature stable H-bond interactions, and also binding free energy nearer to that of the substrate-bound complex of 6PGD than ChemBridge_80178394. Hence, the overall analyses imply that the prioritized compounds ChemBridge_11084819 and ChemBridge_17912340 shall be potent drug moieties for targeting 6PGD to combat malaria caused by Plasmodium species.

Disclosure statement

No conflict of interest was reported by the authors.

Funding

JJ thanks the DST INDO-TAIWAN (GITA/DST/TWN/P-86/2019), Department of Biotechnology-Bioinformatics Centre (BIC)-No.BT/PR40154/BTIS/137/34/2021, TANSCHE (RGP/2019-20/ALU/HECP-0049 dated:27/04/2021), DBT-NNP-N0.BT/PR40156/BTIS/137/54/2023, DST-Fund for Improvement of S&T Infrastructure in Universities & Higher Educational Institutions (FIST) (SR/FST/LSI-667/2016) (C), and DST-Promotion of University Research and Scientific Excellence (PURSE phase II) (No. SR/PURSE Phase 2/38 (G), 2017) for the financial support and facilities. CJ Chen greatly acknowledges MOST 107-2923-B-213-001-MY3 and MOST 108-2311-B-213-001-MY3 for providing financial assistance through Major Research Projects. NH greatly acknowledges the Department of Science and Technology (DST), for providing financial assistance through DST/INSPIRE Fellowship/2019/IF190083. The authors thank Vision Research Foundation, Chennai for providing a computational facility. AM, sincerely thank ICMR – Senior Research Fellowship (107/2022-ECD-II dated 01/11/22) for providing financial assistance.

References

AIP Conference Proceedings. (1992). AIP.

Aly, A. S., Vaughan, A. M., & Kappe, S. H. (2009). Malaria parasite development in the mosquito and infection of the mammalian host. *Annual Review of Microbiology*, *63*, 195–221. https://doi.org/10.1146/annurev.micro.091208.073403

Amala, M., Rajamanikandan, S., Prabhu, D., Surekha, K., & Jeyakanthan, J. (2019). Identification of anti-filarial leads against aspartate semialdehyde dehydrogenase of Wolbachia endosymbiont of Brugia malayi: Combined molecular docking and molecular dynamics approaches. *Journal of Biomolecular Structure & Dynamics*, *37*(2), 394–410. https://doi.org/10.1080/07391102.2018.1427633

Antinori, S., Galimberti, L., Milazzo, L., & Corbellino, M. (2012). Biology of human malaria plasmodia including *Plasmodium knowlesi*. *Mediterranean Journal of Hematology and Infectious Diseases*, *4*(1), e2012013. https://doi.org/10.4084/MJHID.2012.013

Ayala, A., Fabregat, I., & Machado, A. (1991). The role of NADPH in the regulation of glucose-6-phosphate and 6-phosphogluconate dehydrogenases in rat adipose tissue. *Molecular and Cellular Biochemistry*, *105*(1), 1–5. https://doi.org/10.1007/BF00230368

Becke, A. D. (1993). Density-functional thermochemistry. III. The role of exact exchange. *Journal of Chemical Physics*, *98*(7), 5648–5652. https://doi.org/10.1063/1.464913

Becker, K., Tilley, L., Vennerstrom, J. L., Roberts, D., Rogerson, S., & Ginsburg, H. (2004). Oxidative stress in malaria parasite-infected erythrocytes: Host-parasite interactions. *International Journal for Parasitology*, *34*(2), 163–189. https://doi.org/10.1016/j.ijpara.2003.09.011

Boros, L. G., Brandes, J. L., Yusuf, F. I., Cascante, M., Williams, R. D., & Schirmer, W. J. (1998). Inhibition of the oxidative and nonoxidative pentose phosphate pathways by somatostatin: A possible mechanism of antitumor action. *Medical Hypotheses*, *50*(6), 501–506. https://doi.org/10.1016/s0306-9877(98)90271-7

Caliandro, R., Rossetti, G., & Carloni, P. (2012). Local Fluctuations and conformational transitions in proteins. *Journal of Chemical Theory and Computation*, *8*(11), 4775–4785. https://doi.org/10.1021/ct300610y

Çalışkan, B., Öztürk Kesebir, A., Demir, Y., & Akyol Salman, İ. (2022). The effect of brimonidine and proparacaine on metabolic enzymes: Glucose-6-phosphate dehydrogenase, 6-phosphogluconate dehydrogenase, and glutathione reductase. *Biotechnology and Applied Biochemistry*, *69*(1), 281–288. https://doi.org/10.1002/bab.2107

Chen, L., Zhang, Z., Hoshino, A., Zheng, H. D., Morley, M., Arany, Z., & Rabinowitz, J. D. (2019). NADPH production by the oxidative pentose-phosphate pathway supports folate metabolism. *Nature Metabolism*, *1*(3), 404–415. https://doi.org/10.1038/s42255-019-0043-x

Choubey, S. K., & Jeyaraman, J. (2016). A mechanistic approach to explore novel HDAC1 inhibitor using pharmacophore modeling, 3D-QSAR analysis, molecular docking, density functional and molecular dynamics simulation study. *Journal of Molecular Graphics & Modelling*, *70*, 54–69. https://doi.org/10.1016/j.jmgm.2016.09.008

Cowell, A. N., & Winzeler, E. A. (2019). The genomic architecture of antimalarial drug resistance. *Briefings in Functional Genomics*, *18*(5), 314–328. https://doi.org/10.1093/bfgp/elz008

Dhangadamajhi, G., Kar, S. K., & Ranjit, M. (2010). The survival strategies of malaria parasite in the red blood cell and host cell polymorphisms. *Malaria Research and Treatment*, *2010*, 973094. https://doi.org/10.4061/2010/973094

Dixon, S. L., Smondyrev, A. M., Knoll, E. H., Rao, S. N., Shaw, D. E., & Friesner, R. A. (2006). PHASE: A new engine for pharmacophore perception, 3D QSAR model development, and 3D database screening: 1. Methodology and preliminary results. *Journal of Computer-Aided Molecular Design*, *20*(10–11), 647–671. https://doi.org/10.1007/s10822-006-9087-6

Dixon, S. L., Smondyrev, A. M., & Rao, S. N. (2006). PHASE: A novel approach to pharmacophore modeling and 3D database searching. *Chemical Biology & Drug Design*, *67*(5), 370–372. https://doi.org/10.1111/j.1747-0285.2006.00384.x

Friesner, R. A., Banks, J. L., Murphy, R. B., Halgren, T. A., Klicic, J. J., Mainz, D. T., Repasky, M. P., Knoll, E. H., Shelley, M., Perry, J. K., Shaw, D. E., Francis, P., & Shenkin, P. S. (2004). Glide: A new approach for rapid, accurate docking and scoring. 1. Method and assessment of docking accuracy. *Journal of Medicinal Chemistry*, *47*(7), 1739–1749. https://doi.org/10.1021/jm0306430

Friesner, R. A., Murphy, R. B., Repasky, M. P., Frye, L. L., Greenwood, J. R., Halgren, T. A., Sanschagrin, P. C., & Mainz, D. T. (2006). Extra precision glide: Docking and scoring incorporating a model of hydrophobic enclosure for protein-ligand complexes. *Journal of Medicinal Chemistry*, *49*(21), 6177–6196. https://doi.org/10.1021/jm051256o

Gregson, A., & Plowe, C. V. (2005). Mechanisms of resistance of malaria parasites to antifolates. *Pharmacological Reviews*, *57*(1), 117–145. https://doi.org/10.1124/pr.57.1.4

Haeussler, K., Berneburg, I., Jortzik, E., Hahn, J., Rahbari, M., Schulz, N., Preuss, J., Zapol'skii, V. A., Bode, L., Pinkerton, A. B., Kaufmann, D. E., Rahlfs, S., & Becker, K. (2019). Glucose 6-phosphate dehydrogenase 6-phosphogluconolactonase: Characterization of the Plasmodium vivax enzyme and inhibitor studies. *Malaria Journal*, *18*(1), 22. https://doi.org/10.1186/s12936-019-2651-z

Haeussler, K., Fritz-Wolf, K., Reichmann, M., Rahlfs, S., & Becker, K. (2018). Characterization of plasmodium falciparum 6-phosphogluconate dehydrogenase as an antimalarial drug target. *Journal of Molecular Biology*, *430*(21), 4049–4067. https://doi.org/10.1016/j.jmb.2018.07.030

Halgren, T. A., Murphy, R. B., Friesner, R. A., Beard, H. S., Frye, L. L., Pollard, W. T., & Banks, J. L. (2004). Glide: A new approach for rapid, accurate docking and scoring. 2. Enrichment factors in database screening. *Journal of Medicinal Chemistry*, *47*(7), 1750–1759. https://doi.org/10.1021/jm030644s

Hess, B. (2008). P-LINCS: A parallel linear constraint solver for molecular simulation. *Journal of Chemical Theory and Computation*, *4*(1), 116–122. https://doi.org/10.1021/ct700200b

Humphrey, W., Dalke, A., & Schulten, K. (1996). VMD: Visual molecular dynamics. *Journal of Molecular Graphics*, *14*(1), 33–28. https://doi.org/10.1016/0263-7855(96)00018-5

Huthmacher, C., Hoppe, A., Bulik, S., & Holzhütter, H. G. (2010). Antimalarial drug targets in Plasmodium falciparum predicted by stage-specific metabolic network analysis. *BMC Systems Biology*, *4*(1), 120. https://doi.org/10.1186/1752-0509-4-120

Institute of Medicine (US) Committee on the Economics of Antimalarial Drugs. (2004). *Saving lives, buying time: Economics of malaria drugs in an age of resistance* (Arrow, K. J., Panosian, C., & Gelband, H., Eds.). National Academies Press.

Jaguar. (2021). Schrödinger, LLC, New York, NY

Jorgensen, W. L., & Tirado-Rives, J. (1988). The OPLS [optimized potentials for liquid simulations] potential functions for proteins, energy minimizations for crystals of cyclic peptides and crambin. *Journal of the American Chemical Society*, *110*(6), 1657–1666. https://doi.org/10.1021/ja00214a001

Karaman, M., Temel, Y., & Bayindir, S. (2020). Inhibition effect of rhodanines containing benzene moieties on pentose phosphate pathway enzymes and molecular docking. *Journal of Molecular Structure*, *1220*, 128700. https://doi.org/10.1016/j.molstruc.2020.128700

Karthika, A., Ramachandran, B., Chitra, J., Prabhu, D., Rajamanikandan, S., Veerapandiyan, M., & Jeyakanthan, J. (2021). Molecular dynamics simulation of toxin-antitoxin (TA) system in Acinetobacter baumannii to explore the novel mechanism for inhibition of cell wall biosynthesis: Zeta toxin as an effective therapeutic target. *Journal of Cellular Biochemistry*, *122*(12), 1832–1847. https://doi.org/10.1002/jcb.30137

Kaushansky, A., Metzger, P. G., Douglass, A. N., Mikolajczak, S. A., Lakshmanan, V., Kain, H. S., & Kappe, S. H. (2013). Malaria parasite liver stages render host hepatocytes susceptible to mitochondria-initiated apoptosis. *Cell Death & Disease*, *4*(8), e762. https://doi.org/10.1038/cddis.2013.286

Kesebir, A. Ö., Güller, P., Kalın, R., Özdemir, H., & Küfrevioğlu, Ö. İ. (2022). Methyl benzoate derivatives as inhibitors of pentose phosphate pathway, which promotes cancer progression and drug resistance: An in silico study supported by in vitro results. *Biotechnology and Applied Biochemistry*, *69*(3), 1275–1283. https://doi.org/10.1002/bab.2322

Kim, S., Thiessen, P. A., Bolton, E. E., Chen, J., Fu, G., Gindulyte, A., Han, L., He, J., He, S., Shoemaker, B. A., Wang, J., Yu, B., Zhang, J., & Bryant, S. H. (2016). PubChem substance and compound databases. *Nucleic Acids Research*, *44*(D1), D1202–D1213. https://doi.org/10.1093/nar/gkv951

Lee, C., Yang, W., & Parr, R. G. (1988). Development of the Colle-Salvetti correlation-energy formula into a functional of the electron density. *Physical Review. B, Condensed Matter*, *37*(2), 785–789. https://doi.org/10.1103/physrevb.37.785

Ligprep. (2021). Schrödinger, LLC, New York, NY.

Litwack, G. (2018). *Chapter 8—Glycolysis and gluconeogenesis* (pp. 183–198). Academic Press.

Maisuradze, G. G., Liwo, A., & Scheraga, H. A. (2009). Principal component analysis for protein folding dynamics. *Journal of Molecular Biology*, *385*(1), 312–329. https://doi.org/10.1016/j.jmb.2008.10.018

Nagarajan, H., Samdani, A., Umashankar, V., & Jeyakanthan, J. (2022). Deciphering the conformational transitions of LIMK2 active and inactive states to ponder specific druggable states through microsecond scale molecular dynamics simulation. *Journal of Computer-Aided Molecular Design*, *36*(6), 459–482. https://doi.org/10.1007/s10822-022-00459-0

Nepveu, F., & Turrini, F. (2013). Targeting the redox metabolism of Plasmodium falciparum. *Future Medicinal Chemistry*, *5*(16), 1993–2006. https://doi.org/10.4155/fmc.13.159

Nguyen, T. T., Viet, M. H., & Li, M. S. (2014). Effects of water models on binding affinity: Evidence from all-atom simulation of binding of tamiflu to A/H5N1 neuraminidase. *Scientific World Journal*, *2014*, 536084. https://doi.org/10.1155/2014/536084

Nosten, F., & White, N. J. (2007). Artemisinin-based combination treatment of Falciparum Malaria. In Breman, J. G., Alilio, M. S., & White, N. J. (Ed.), *Defining and defeating the intolerable burden of malaria III: Progress and perspectives: Supplement to volume 77(6) of American Journal of Tropical Medicine and Hygiene*. American Society of Tropical Medicine and Hygiene. https://doi.org/10.4269/ajtmh.2007.77.i

Oostenbrink, C., Villa, A., Mark, A. E., & van Gunsteren, W. F. (2004). A biomolecular force field based on the free enthalpy of hydration and solvation: The GROMOS force-field parameter sets 53A5 and 53A6. *Journal of Computational Chemistry*, *25*(13), 1656–1676. https://doi.org/10.1002/jcc.20090

Özaslan, M. S., Balcı, N., Demir, Y., Gürbüz, M., & Küfrevioğlu, Ö. İ. (2019). Inhibition effects of some antidepressant drugs on pentose phosphate pathway enzymes. *Environmental Toxicology and Pharmacology*, *72*, 103244. https://doi.org/10.1016/j.etap.2019.103244

Pimenta, P. F., Orfano, A. S., Bahia, A. C., Duarte, A. P., Ríos-Velásquez, C. M., Melo, F. F., Pessoa, F. A., Oliveira, G. A., Campos, K. M., Villegas, L. M., Rodrigues, N. B., Nacif-Pimenta, R., Simões, R. C., Monteiro, W. M., Amino, R., Traub-Cseko, Y. M., Lima, J. B., Barbosa, M. G., & Lacerda, M. V. (2015). An overview of malaria transmission from the perspective of Amazon Anopheles vectors. *Memorias Do Instituto Oswaldo Cruz*, *110*(1), 23–47. https://doi.org/10.1590/0074-02760140266

Preuss, J., Jortzik, E., & Becker, K. (2012). Glucose-6-phosphate metabolism in Plasmodium falciparum. *IUBMB Life*, *64*(7), 603–611. https://doi.org/10.1002/iub.1047

Prime. (2021). Schrödinger, LLC, New York, NY.

Protein Preparation Wizard. (2021). Epik version, Schrödinger, LLC, New York, NY

QikProp. (2021). Schrödinger LLC, New York, NY.

Rajamanikandan, S., Jeyakanthan, J., & Srinivasan, P. (2017). Discovery of potent inhibitors targeting Vibrio harveyi LuxR through shape and e-pharmacophore based virtual screening and its biological evaluation. *Microbial Pathogenesis*, *103*, 40–56. https://doi.org/10.1016/j.micpath.2016.12.003

Shibeshi, M. A., Kifle, Z. D., & Atnafie, S. A. (2020). Antimalarial drug resistance and novel targets for antimalarial drug discovery. *Infection and Drug Resistance*, *13*, 4047–4060. https://doi.org/10.2147/IDR.S279433

Stincone, A., Prigione, A., Cramer, T., Wamelink, M. M., Campbell, K., Cheung, E., Olin-Sandoval, V., Grüning, N. M., Krüger, A., Tauqeer Alam, M., Keller, M. A., Breitenbach, M., Brindle, K. M., Rabinowitz, J. D., & Ralser, M. (2015). The return of metabolism: Biochemistry and physiology of the pentose phosphate pathway. *Biological Reviews of the Cambridge Philosophical Society*, *90*(3), 927–963. https://doi.org/10.1111/brv.12140

Surekha, K., Prabhu, D., Richard, M., Nachiappan, M., Biswal, J., & Jeyakanthan, J. (2016). Investigation of vital pathogenic target orotate phosphoribosyltransferases (OPRTase) from Thermus thermophilus HB8: Phylogenetic and molecular modeling approach. *Gene*, *583*(2), 102–111. https://doi.org/10.1016/j.gene.2016.02.006

Van Der Spoel, D., Lindahl, E., Hess, B., Groenhof, G., Mark, A. E., & Berendsen, H. J. (2005). GROMACS: Fast, flexible, and free. *Journal of Computational Chemistry*, *26*(16), 1701–1718. https://doi.org/10.1002/jcc.20291

Wang, L., Pang, X., Li, Y., Zhang, Z., & Tan, W. (2017). RADER: A rapid decoy retriever to facilitate decoy based assessment of virtual screening. *Bioinformatics (Oxford, England)*, *33*(8), 1235–1237. https://doi.org/10.1093/bioinformatics/btw783

WHO Report Malaria. (2020). World Health Organization Media Centre Fact Sheet.

Yıldız, M. L., Demir, Y., & Küfrevioğlu, Ö. I. (2022). Screening of in vitro and in silico effect of fluorophenylthiourea compounds on glucose 6-phosphate dehydrogenase and 6-phosphogluconate dehydrogenase enzymes. *Journal of Molecular Recognition: JMR*, *35*(12), e2987. https://doi.org/10.1002/jmr.2987